Continental Shelf Research 226 (2021) 104486

Contents lists available at ScienceDirect

Continental Shelf Research

journal homepage: www.elsevier.com/locate/csr

Research papers

A diagnosis of surface currents and sea surface heights in a coastal region

Eun Ae Lee, Sung Yong Kim *

Environmental Fluid Mechanics Laboratory, Department of Mechanical Engineering, Korea Advanced Institute of Science and Technology, 291 Daehak-ro, Yuseong-gu, Daejeon 34141, Republic of Korea

ARTICLE INFO

Keywords:
Geostrophic currents
Ageostrophic currents
Degree of geostrophy
Degree of geostrophic imbalance
Sea surface heights
Surface currents

ABSTRACT

Upcoming satellite missions will observe the sea surface height (SSH) fields at a very high spatial resolution, which has generated an urgent need to better understand how well geostrophy can represent the ocean current field at finer scales, particularly in coastal regions characterized by complex flow geometry. We conduct statistical and spectral analyses of high-resolution surface currents and SSHs off the Oregon coast to examine the relative contribution of geostrophy and ageostrophy in coastal ocean currents. We analyze forward numerical simulations based primarily on a regional ocean model (ROMS) and use regional observations of high-frequency radar (HFR)-derived surface currents and altimeter-derived geostrophic currents and a subset of global domain numerical simulations (MITgcm) as secondary resources. Regional submesoscale ageostrophic currents account for up to 50% of the total variance and are primarily associated with near-inertial currents and internal tides. Geostrophy becomes dominant at time scales longer than 3 to 10 days and at spatial scales longer than 50 km, and is dependent on the depth and distance from the coast in the cross-shore direction. Ageostrophy dominates in the near-inertial and super-inertial frequency bands, which correspond to near-inertial motions (Coriolis force dominates) and high-frequency internal waves/tides (pressure gradient dominates), respectively. Because of ageostrophy, it may not be possible to estimate submesoscale currents from SSHs obtained from upcoming satellite missions using the geostrophic relationship. Thus, other concurrent high-resolution in-situ observations such as HFR-derived surface currents, together with data assimilation techniques, should be used for constructive data integration to resolve submesoscale currents.

1. Introduction

Oceanic submesoscale processes are characterized by (1) horizontal scales smaller than the first baroclinic Rossby deformation radius [$O(1)$ km to $O(100)$ km], (2) temporal scales in a range of $O(1)$ hour to a few days, and (3) dominance of the vertical component of relative vorticity relative to planetary vorticity (e.g., McWilliams, 2016; Kim, 2010; Soh and Kim, 2018; Yoo et al., 2018; Lee and Kim, 2018). These processes have received much attention as a result of their importance to physical and biological and biogeochemical processes in the ocean, such as their contributions to the vertical transport of oceanic tracers, mass, nutrients, and buoyancy, their influence on mixed-layer structures and upper ocean stratification, and their influence on the productivity and diversity of marine ecosystems (e.g., Thomas et al., 2008; Omand et al., 2015; Lévy et al., 2018). Limited submesoscale observations are available because the temporal and spatial scales of submesoscale processes make them difficult to obtain using traditional *in-situ* observational techniques (e.g., Kim, 2010; D'Asaro et al., 2011; Shcherbina et al., 2013; Buckingham et al., 2016).

Operational high-resolution satellite observations of submesoscale processes have been initiated to overcome the limitations of present-day satellite sensors (e.g., Stammer, 1997; Chavanne and Klein, 2010), including the Surface Water and Ocean Topography (SWOT) mission (e.g., Fu and Ferrari, 2008; Fu, 2010; Durand et al., 2010), the Coastal and Ocean Measurement mission with Precise and Innovative Radar Altimeter (COMPIRA) (e.g., Uematsu et al., 2013), the SEASTAR mission (e.g., Gommenginger and Chapron, 2018; Gommenginger et al., 2019), the Sea Surface KInematics Multiscale monitoring (SKIM) mission (e.g., Ardhuin et al., 2018), and the Winds and Currents Mission (WaCM) (e.g., Rodriguez et al., 2018). For instance, the submesoscale sea surface heights (SSHs) obtained from these operational satellite missions represent an important resource for investigating not only ocean (geostrophic) circulations (e.g., Gill, 1982; Chelton and Schlax, 2003) but also submesoscale processes, and internal waves and tides (e.g., Alpers, 1985; Ponte and Klein, 2015). However, it can be challenging to determine to what extent and how well submesoscale ocean circulations can be retrieved from high-resolution satellite SSH observations.

* Corresponding author.
E-mail address: syongkim@kaist.ac.kr (S.Y. Kim).

https://doi.org/10.1016/j.csr.2021.104486
Received 5 May 2020; Received in revised form 3 June 2021; Accepted 18 June 2021
Available online 23 June 2021

High-resolution SSH data may contain both geostrophic components and ageostrophic components (e.g., Errico, 1980; Rocha et al., 2016a; Qiu et al., 2018) and include the signals of both barotropic and baroclinic tides (e.g., Ray and Cartwright, 2001), except for the signals related to inertial motions (e.g., Klein et al., 2009; Verdy et al., 2013). The ageostrophic components include stationary and non-stationary internal tides, non-tidal inertia-gravity waves (IGWs), near-inertial motions, frictional effects, mixed-layer instabilities, fronts, and filaments (e.g., Rossby, 1938; Veronis, 1956; Blumen, 1967; Errico, 1980; Ray and Cartwright, 2001; Williams et al., 2008; Rocha et al., 2016a). Thus, the complete retrieval of submesoscale processes and circulations from satellite-derived submesoscale SSHs can be a challenge in observational submesoscale studies. For instance, Ubelmann et al. (2015) examined the possibility to extract dynamical components from submesoscale SSH observations using wavenumber-domain coherence and dynamic interpolation (e.g., potential vorticity equation). Forget and Ponte (2015) extensively investigated ways to decompose SSHs into large-scale/mesoscale SSHs and residuals using scales, physical processes, and forcing-response mechanisms as well as quantification of the signal and noise associated with these decompositions, which provides comprehensive views in extracting meaningful signals from observations. Retrieving small-scale SSH observations and performing relevant field reconstructions from the SWOT mission data can be limited to spatial scales longer than 85 km, based on a comparison of both spectra of SWOT-mapped SSHs and true SSHs, and may require more information on the vertical structure of the ocean (e.g., Gaultier et al., 2016; Wang et al., 2018).

In recent submesoscale process studies, high-frequency radar (HFR)-derived surface currents, which are the currents averaged over the upper ocean to a depth of $O(1)$ m at an hourly temporal resolution and $O(1)$ km spatial resolution, have been increasingly used because of their pertinence to submesoscale coastal circulation studies (e.g., Gildor et al., 2009; Kim, 2010; Yoo et al., 2018; Soh and Kim, 2018; Lai et al., 2017; Archer et al., 2020). The HFR-derived surface currents contain variance that corresponds to local and remote winds, tides, near-inertial motions, and submesoscale eddies and fronts (e.g., Kim et al., 2011, 2013; Kim and Kosro, 2013).

Satellite-derived high-resolution SSHs and HFR-derived submesoscale surface currents would be valuable resources for submesoscale process studies, and extraction of the dynamic components from them via integrated data analysis can be complementary. Moreover, submesoscale numerical simulations can be used as resources to illustrate whether high-resolution satellite altimetry can capture the full velocity field at the submesoscale, including ageostrophic components. Thus, in this paper, we (1) present the variance in surface currents and SSHs in the observations using HFRs and altimeters and in submesoscale numerical model simulations using the Regional Ocean Modeling System (ROMS) and Massachusetts Institute of Technology general circulation model (MITgcm) (Section 2) and (2) delineate the coastal submesoscale surface currents into the geostrophic and ageostrophic components (Sections 3 and 4). A discussion and summary follow in Sections 5 and 6, respectively.

2. Data

2.1. Study domain

A study domain is divided into five subdomains (D1, D2, D3, D4, and D5) for detailed investigations (Fig. 1a): a cross-shore line at 44.65°N as a cross-shore extension of the Newport Hydrographic (NH) line (D1), two 1° square boxes in the coastal and offshore regions centered over the NH line (D2 and D3), and two cross-shore bands centered over the NH line with a width of 0.25° and 3° (D4 and D5). A coastal region in the northeastern Pacific is chosen as the study domain because (1) two numerical model simulations (Section 2.2) and observations of HFR-derived submesoscale coastal surface currents and altimetry-derived sea surface height anomalies (SSHAs) and geostrophic currents (Section 2.3) are available, (2) there is a clear separation of the variance between local inertial frequency and two primary tides (K_1 and M_2) (e.g., Kim and Kosro, 2013), and (3) the coastal circulation can be described in a relatively simple way associated with a nearly straight coastline. A green box in Fig. 1b shows a coastal area where the HFR-derived and ROMS-simulated surface currents were sampled to estimate their azimuthally averaged wavenumber–frequency-domain power spectral density function (hereafter referred to as energy spectra).

In this coastal region, the seasonal wind–current dynamics over the continental shelf are characterized by spring upwelling, fall relaxation, and winter down-welling as a part of the California Current System (e.g., Strub et al., 1987; Largier et al., 1993; Strub and James, 2000). Additionally, intermittently poleward propagating along-shore currents/waves (Chapman, 1987; Kim et al., 2013), barotropic and baroclinic tides (e.g., Osborne et al., 2011, 2014), and onshore propagated near-inertial motions and their coastal inhibition under seasonally and vertically stratified conditions associated with Columbia river flows (e.g., Kim et al., 2014) have been observed. Off the Oregon coast, the first baroclinic Rossby radius of deformation is in a range of 20 km to 30 km (e.g., Chelton et al., 1998). Under these regional characteristics, we can generalize outcomes of this paper to any coastal regions having seasonal wind–current dynamics. Moreover, some outcomes as site-specific characteristics will be discussed in Section 5.4.

2.2. Numerical model outputs

We analyze the surface currents and SSHs off the Oregon coast in two different and forward numerical simulation outputs obtained from the ROMS and MITgcm (llc4320 product).

In the ROMS, the regional domain extends from 40.6°N to 50°N and from 130°W to the coast (approximately 450 km in cross-shore distance), and the model resolution is 2 km in the horizontal direction and 40 terrain-following layers in the vertical direction, with relatively better resolution near the surface and bottom. Atmospheric forcing obtained from the National Oceanic and Atmospheric Administration North American Model (NOAA NAM), subtidal boundary conditions obtained from the 1/12° data assimilating Hybrid Coordinate Ocean Model (HYCOM), and eight primary barotropic tides at the open boundaries are applied under the hydrostatic assumption. The model outputs are archived for a period of approximately one year (August 2008 to August 2009) (see Kim et al., 2014, 2015b; Osborne et al., 2011, 2014 for more details).

The MITgcm llc4320 global model is forced by the ERA Interim wind stress and primary tidal constituents under the non-hydrostatic assumption (e.g., Marshall et al., 1997; Forget et al., 2015; Qiu et al., 2018). The model resolution is 1/48° (approximately 1.5 km) in the horizontal direction and 86 z-coordinate layers in the vertical direction. The simulation was conducted for approximately one year (September 13, 2011 to November 15, 2012). The global model outputs are regionally subsampled within the ROMS domain without any interpolation, maintaining the original spatial and temporal resolutions.

Although the horizontal and vertical grid points in the two numerical model simulations are configured differently, the u- and v-components of both model currents are linearly interpolated to the center of each grid cell because they are provided non-collocatedly on the sides of each computational cell under the staggered Arakawa 'C' grid (e.g., Arakawa, 1966).

The ROMS outputs used in this paper simulate regional coastal circulations and variability in a manner that is dynamically and statistically consistent with observations, including low-frequency currents (e.g., coastal trapped waves), near-inertial currents, and tidal currents (e.g., Kim et al., 2014, 2015b; Osborne et al., 2011, 2014). In addition, the MITgcm in the same coastal region can provide not only another

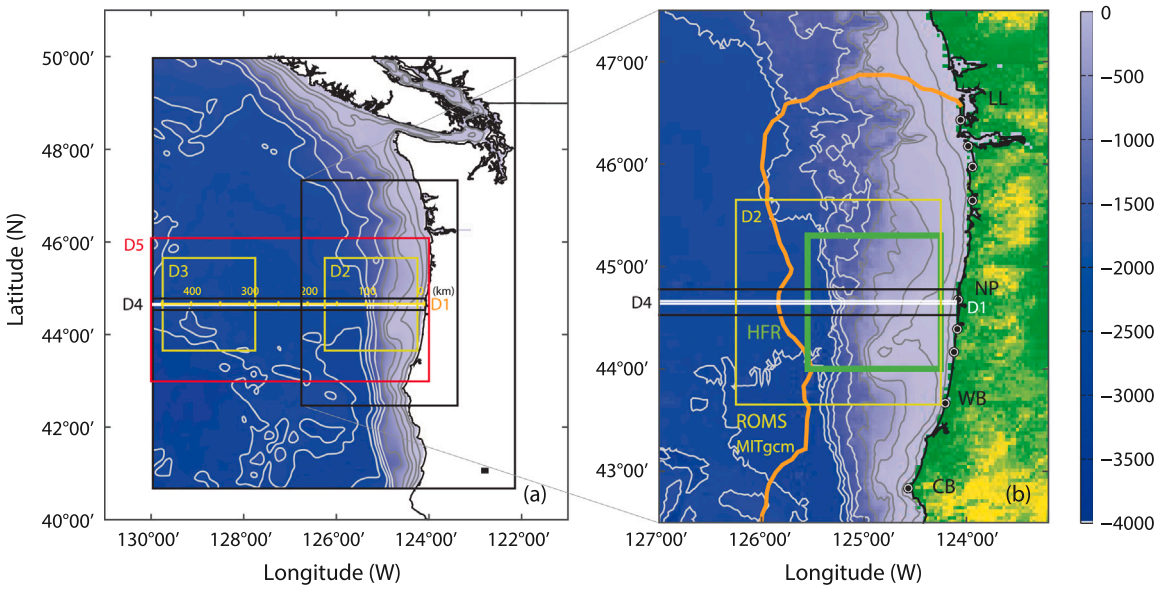

Fig. 1. (a) A domain for numerical simulations using ROMS and MITgcm, ranging from 130°W to the coast and between 40.6°N and 50°N for the study of submesoscale coastal surface currents and high-resolution sea surface heights (SSHs) off the coast of Oregon. Five sub-domains for detailed investigations (D1, D2, D3, D4, and D5) are used. An example of 5 by 5 ROMS model grid points with a spatial resolution of 2 km is shown in the bottom right corner. (b) A close-up of the near coast region to overlap the ROMS and MITgcm simulations (a light green box; D2) and HFR-derived surface current observations (an orange contour and a green box) where the azimuthally averaged wavenumber–frequency-domain energy spectra are estimated (see Fig. 4). As a reference, major coastal regions are denoted by abbreviated two-letter names from south to north: Cape Blanco (CB), Winchester Bay (WB), Newport (NP), and Loomis Lake (LL). The bottom bathymetry in Fig. 1a and b is contoured at 50 m, 100 m, 250 m, 500 m, 1000 m, 1500 m, 2000 m, 2500 m, and 3000 m.

view on the z-coordinate regional simulation but also comprehensive perspectives, including the dynamical decomposition on the submesoscale SSHs and surface currents obtained from upcoming satellite missions by connecting this work into the companion paper (Lee and Kim, 2021) in a context of the previous studies using MITgcm submesoscale simulations (e.g., Rocha et al., 2016a,b; Savage et al., 2017a; Uchida et al., 2017; Torres et al., 2018; Qiu et al., 2018; Chereskin et al., 2019; Dong et al., 2020). However, the numerical model outputs do not exactly duplicate the actual observations in time and space. Thus, we analyzed the numerical model outputs via statistical and spectral analyses and compared the results with observations to discuss their differences and potential limitations. The main presentations in this paper are based on the ROMS outputs. Physically significant differences between the two models' outputs will be noted.

2.3. Observations

To compare the two numerical model outputs described above with observations, we analyze three sets of observations off Oregon for a period of four years (2007 to 2010): the optimally interpolated (OI) AVISO daily geostrophic currents and SSHAs on a quarter-degree grid and the OI-mapped HFR-derived hourly surface currents on a 6 km grid (a green box in Fig. 1b) (e.g., Kosro, 2005; Kim and Kosro, 2013; Kim et al., 2014, 2015b). An operational compact array system off the Oregon coast consists of 5 MHz (8 stations) and 13 MHz (7 stations) HFRs. The wavenumber-domain energy spectra of the HFR-derived surface currents follow the theoretical slopes of geophysical turbulent flows (e.g., submesoscale) without any features of sharp drops or noise floor and continuously decays toward high wavenumber (e.g., Kim et al., 2011; Soh and Kim, 2018). In the southern California coast, the HFR-derived surface currents mapped on a 6 km grid obtained from 5 MHz and 13 MHz HFRs have significantly lower variance at the spatial scale of 10 to 40 km than those mapped on a 1-km grid obtained from 25 MHz HFRs (e.g., Kim et al., 2011). Since a similar observational system has been in operation off the Oregon coast, the effective spatial resolution is approximately 20 to 30 km (see Section 4.1 for more details; see Ballarotta et al., 2019 for mathematical definitions of the effective resolution). On the contrary, the effective spatial resolution of the OI-mapped AVISO geostrophic currents has been reported in a range of 100 to 200 km because the satellite altimetry has the observational limitation below 100 km spatial scale (e.g., Stammer, 1997; Soh and Kim, 2018; Chelton et al., 2019; Ballarotta et al., 2019).

3. Methods

3.1. Estimates of spectral content of currents and SSHs

3.1.1. Frequency domain and cross-shore distance

The (rotary) energy spectra $[S(\sigma, x)]$ in the frequency (σ) and cross-shore distance (x) are estimated with a meridional average of individual energy spectra as follows:

$$S(\sigma, x) = \frac{1}{N}\sum_{n=1}^{N} S(\sigma, x, y_n), \tag{1}$$

where N indicates the number of alongshore grid points ($n = 1, \ldots, N$),

$$S(\sigma, x, y_n) = \frac{1}{\Delta\sigma}\left|\frac{1}{R}\sum_{r=1}^{R} d(t_r, x, y_n)e^{-i\sigma t_r}\right|^2, \tag{2}$$

R denotes the number of realizations ($r = 1, \ldots, R$), the vector components (u and v) of HFR-derived surface currents, ROMS-simulated surface currents, and AVISO-derived geostrophic currents are combined with a complex number ($d = u + iv$).

The rotary energy spectra of the vector time series combined with a complex number ($u + iv$) represent the rotational dominance in positive (counter-clockwise) and negative (clockwise) frequency bands (e.g., Emery and Thomson, 1997; Walden, 2013). The sum of the rotary variance at each frequency in both rotations is identical to the sum of the energy spectra of individual velocity components (u and v) at each frequency.

3.1.2. Frequency and cross-shore wavenumber domains

The (rotary) energy spectra $[S(\sigma,k)]$ in the frequency and cross-shore wavenumber domains are averaged in the alongshore direction (y) as follows:

$$S(\sigma,k)=\frac{1}{N}\sum_{n=1}^{N}S(\sigma,k,y_n), \tag{3}$$

where

$$S(\sigma,k,y_n)=\frac{1}{\Delta\sigma}\frac{1}{\Delta k}\left|\frac{1}{R}\frac{1}{M}\sum_{r=1}^{R}\sum_{m=1}^{M}d(t_r,x_m,y_n)e^{-i\sigma t_r-ikx_m}\right|^2, \tag{4}$$

and M denotes the number of cross-shore grid points ($m=1,\dots,M$).

The rotary spectral content in the positive wavenumber and negative wavenumber can be interpreted ambiguously, unlike the interpretation of the frequency-domain rotary spectra. As the temporal axis typically increases forward (e.g., from past to present), the vector time series can be interpreted as predominantly rotating clockwise or counter-clockwise in time. However, as the spatial axis can be defined in various ways (e.g., north to south or south to north, onshore to offshore or offshore to onshore, etc.), it is difficult to interpret the spectral content in the negative wavenumber. Thus, energy spectra in the positive wavenumber and negative wavenumber can be added wavenumber by wavenumber to estimate the total energy spectrum in the (positive) wavenumber, or they are left as they are to highlight any dispersion relationship in the frequency–wavenumber domain, such as the two-dimensional energy spectrum presented in this paper.

3.1.3. Frequency and horizontal wavenumber domains

The azimuthally averaged energy spectra $[S(\sigma,\mathrm{k})]$ are presented in the frequency (σ) and horizontal wavenumber (k; $\mathrm{k}=\mathrm{k}_p$, $p=1,2,\dots,P$) domains,

$$S(\sigma,\mathrm{k}_p)=\frac{1}{\mathcal{K}(\mathrm{k}_p)}\sum S(\sigma,k,l)\Delta\mathrm{k}, \tag{5}$$

where

$$S(\sigma,k,l)=\frac{1}{\Delta\sigma}\frac{1}{\Delta k}\frac{1}{\Delta l}\left|\frac{1}{R}\frac{1}{M}\frac{1}{N}\sum_{r=1}^{R}\sum_{m=1}^{M}\sum_{n=1}^{N}d(t_r,x_m,y_n)e^{-i\sigma t_r-ikx_m-ily_n}\right|^2, \tag{6}$$

and $\mathcal{K}=\mathcal{K}(\mathrm{k}_p)$ is the number of wavenumber grid points within annulus ($\Delta\mathrm{k}$) in the two-dimensional wavenumber domain (k, l). The finite wavenumber axis is defined as

$$\mathrm{k}_p=(p-1)\,\Delta\mathrm{k}, \tag{7}$$

and the number of wavenumber grid points is counted with the condition as follows,

$$\{\mathcal{K}(\mathrm{k}_p)|\mathrm{k}_p-\frac{\Delta\mathrm{k}}{2}<k_h\le\mathrm{k}_p+\frac{\Delta\mathrm{k}}{2}\} \tag{8}$$

and $k_h=\sqrt{k^2+l^2}$.

In practice, the Fourier coefficients of a single vector current map in the k and l domains are Fourier transformed into the frequency domain. Their squared values are then averaged in the finite wavenumber domain (k). Square sampling boxes are considered as long as the available observations are optimally utilized to minimize the directional biases.

Note that we do not present the azimuthally averaged energy spectra as variance-preserving energy spectrum, different from other literature (e.g., Torres et al., 2018) because we avoid potentially misleading interpretation on variance at high wavenumber and high frequency.

3.1.4. Cross-shore distance and alongshore wavenumber

Similarly, the (rotary) energy spectra $[S(x,l)]$ in the cross-shore distance (x) and alongshore wavenumber (l) can be estimated with a temporal average of individual energy spectra as follows:

$$S(x,l)=\frac{1}{R}\sum_{r=1}^{R}S(t_r,x,l), \tag{9}$$

where R denotes the number of realizations ($r=1,\dots,R$), and

$$S(t_r,x,l)=\frac{1}{\Delta l}\left|\frac{1}{N}\sum_{n=1}^{N}d(t_r,x,y_n)e^{-ily_n}\right|^2. \tag{10}$$

3.1.5. Practical remarks on spectral estimates

For more detailed descriptions of the variance estimates (Eqs. (1), (3), and (5)), the Fourier coefficients in the frequency domain are computed using the multiple chunks of non-overlapped time series at a given location to increase the statistical confidence and degrees of freedom of the estimates. Thus, the minimum and maximum values of the frequency ranges of the two data sets can be different (Fig. 4). Moreover, as the azimuthal wavenumber bin is chosen to best estimate the variance and minimize the variance spread, the minimum values of the wavenumber axis can be different in the given data sets (e.g., observations and two different numerical model outputs). The minimum value of the wavenumber axis depends on the domain sizes of the two data sets (Fig. 1b). The jackknife method is applied to evaluate the statistical significance of spectral estimates as part of the sensitivity test (e.g., Emery and Thomson, 1997).

The given data sets of the surface currents and SSHs are described as time series of spatial maps. Thus, these spatial maps of time series are detrended in space or time prior to applying a window function according to the characteristics of the data to minimize the biases at low wavenumber or low frequency, respectively. Moreover, Fourier analysis assumes that the given data are infinitely repeated in the sampled domain. Thus, we apply a Hanning window function to the current and SSH fields sampled in the non-periodic coastal areas for the estimates of energy spectra; this prevents low-frequency variance from contaminating the estimates (e.g., Fu, 1983; Stammer, 1997; Soh and Kim, 2018; Chelton et al., 2019). Although the use of the window function can reduce the original variance, it will produce unambiguous estimates in the spectral decay slope of the wavenumber-domain energy spectra (e.g., Harris, 1978; Priestley, 1981). A more detailed discussion on the use of window functions in the context of the spatial homogeneity and temporal stationarity of the data will be discussed in Section 5.1, including an example of the sensitivity test.

3.2. Delineation of geostrophy and ageostrophy

3.2.1. Geostrophic and ageostrophic currents

Using the geostrophic balance, the geostrophic currents $[\mathbf{u}_g=(u_g,v_g)]$ can be estimated from the spatial gradients of SSHs,

$$u_g(x,y)=-\frac{g}{f_c}\frac{\partial\eta(x,y)}{\partial y}, \tag{11}$$

$$v_g(x,y)=\frac{g}{f_c}\frac{\partial\eta(x,y)}{\partial x}, \tag{12}$$

where g denotes the gravitational acceleration (e.g., Gill, 1982; Chelton and Schlax, 2003). The geostrophic balance is valid only under the assumption of a negligible acceleration term in the momentum equation, which is only valid within a specific frequency and wavenumber band. For instance, a black box in Fig. 3a is the frequency and wavenumber band to satisfy the geostrophic balance as the temporal scale [$|\sigma|\le 0.5$ cycles per day (cpd); $T\ge 2$ days] and spatial scale ($k_h\le 0.01$ km^{-1}; $\lambda\ge 100$ km), which (Sasaki et al., 2014) examined. Thus, the geostrophic currents can be estimated by band-pass filtering of the specific frequency and wavenumber band where significant variance

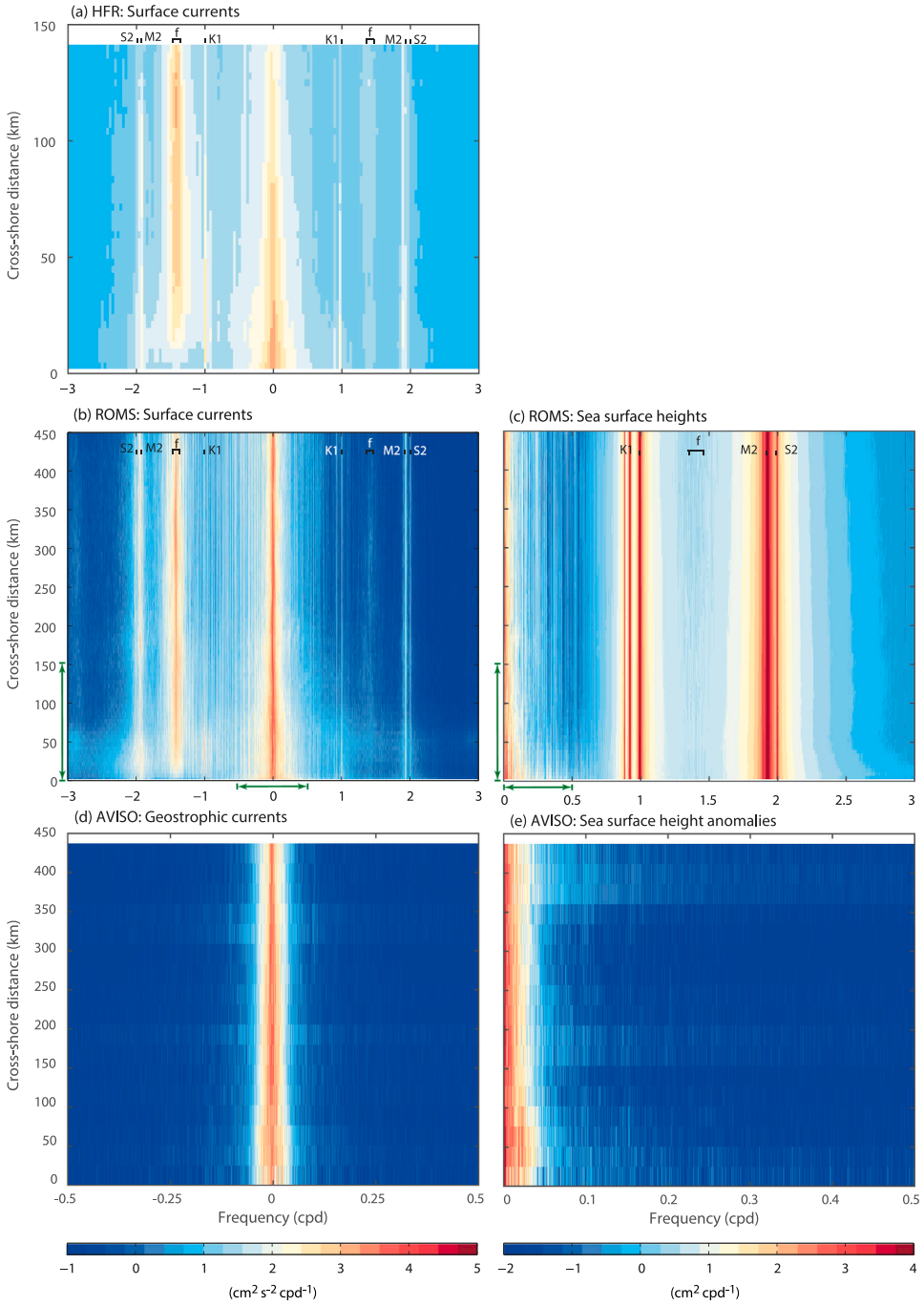

Fig. 2. Alongshore averaged rotary energy spectra [$\log_{10}$ scale; $cm^2 s^{-2} cpd^{-1}$ for (a), (b), and (d); $cm^2 cpd^{-1}$ for (c) and (e)] of the (a) HFR-derived surface currents, (b) ROMS-simulated surface currents, (c) ROMS-simulated SSHs, (d) AVISO geostrophic currents, and (e) AVISO SSHAs in D4. Fig. 2a was modified from Figure 1d in Kim et al. (2011). Green arrows on both axes in Fig. 2b correspond to the cross-shore distance in Fig. 2a and the frequency axis in Fig. 2d.

appears in the kinetic energy spectra (e.g., the green ellipse in Fig. 3a; $|\sigma| \leq 0.2$ cpd and all wavenumbers). The baroclinic components in the geostrophic currents, which are associated with horizontal surface density gradients, are not included in Eqs. (11) and (12) because their amplitudes in the study domain are negligible (see Appendix B for more details).

In contrast, the ageostrophic currents [$\mathbf{u}_{ag} = (u_{ag}, v_{ag})$] in coastal regions are defined from (total) currents [$\mathbf{u} = (u, v)$] and geostrophic currents,

$$u_{ag}(x, y, z) = u(x, y, z) - u_g(x, y), \tag{13}$$

$$v_{ag}(x, y, z) = v(x, y, z) - v_g(x, y). \tag{14}$$

The partitioning of geostrophy and ageostrophy was initially described using balanced geostrophic currents (and Rossby waves) and unbalanced ageostrophic components as the pathways of wind energy injected into the stratified ocean (e.g., Rossby, 1938; Veronis, 1956; Errico, 1980). The dominance of geostrophy and ageostrophy in ocean currents has been described as the regional transition of currents between offshore and nearshore regions (e.g., Kundu et al., 1983; Brink et al., 1991). For example, cross-shore pressure gradients associated with wind-driven onshore transport in coastal regions generate geostrophic currents near the coast in the direction of wind

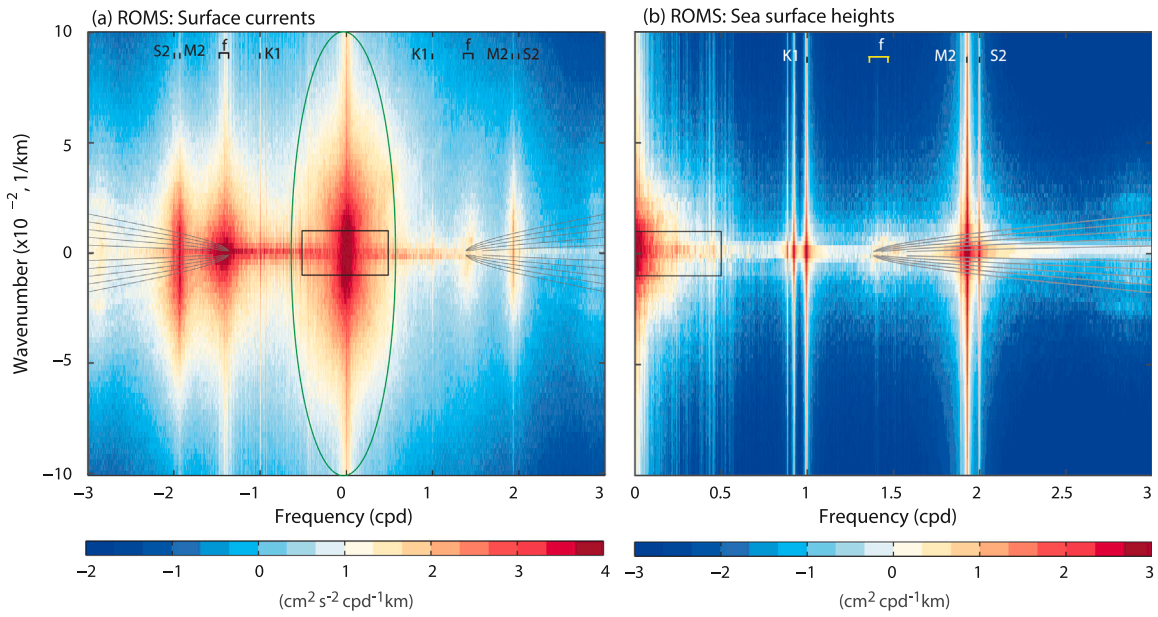

Fig. 3. Alongshore averaged energy spectrum in the wavenumber and frequency domains of the (a) ROMS-simulated surface currents ($\log_{10}$ scale, cm^2 s^{-2} cpd^{-1} km) and (b) ROMS-simulated SSHs ($\log_{10}$ scale; cm^2 s^{-2} cpd^{-1}) on the NH line (D1). The dispersion relationship of IGWs at the first five vertical modes is marked with gray curves in Fig. 3a and b. Black boxes in Fig. 3a and b indicate the temporal scale ($|\sigma| \leq 0.5$ cpd; $T \geq 2$ days) and spatial scale ($k_h \leq 0.01$ km^{-1}; $\lambda \geq 100$ km), which (Sasaki et al., 2014) examined. A green ellipse in Fig. 3a indicates a frequency and wavenumber band which significant variance appears.

stress; the influence of this wind-driven cross-shore transport becomes dominant near the coast but weak offshore (e.g., Csanady, 1982; Minato, 1983; Kim et al., 2015a). On the other hand, the balanced geostrophic currents and unbalanced ageostrophic currents can be decomposed in the spectral domain using the frequency-domain bandpass filter (e.g., Richman et al., 2012) and azimuthally averaged horizontal wavenumber–frequency-domain bandpass filter (e.g., Qiu et al., 2018).

3.2.2. Degrees of geostrophy and geostrophic imbalance

The divergence equation is formulated from the two-dimensional momentum equations, excluding the high order terms $\left[\nabla_h \cdot \left(\nu \nabla_h^2 \mathbf{u}\right)\right]$, as follows:

$$\frac{\partial \delta}{\partial t} + \nabla_h \cdot \left[\left(\mathbf{u} \cdot \nabla_h\right)\mathbf{u}\right] = f_c \zeta - g\nabla_h^2 \eta, \tag{15}$$

where

$$\delta = \nabla_h \cdot \mathbf{u} = \frac{\partial u}{\partial x} + \frac{\partial v}{\partial y}, \tag{16}$$

$$\zeta = \nabla_h \times \mathbf{u} = \frac{\partial v}{\partial x} - \frac{\partial u}{\partial y}, \tag{17}$$

$$\nabla_h = \frac{\partial}{\partial x}\mathbf{i} + \frac{\partial}{\partial y}\mathbf{j}. \tag{18}$$

The degree of geostrophy (κ) is defined as a normalized magnitude of residuals in the balance between the Coriolis force ($f_c\zeta$) and pressure gradients ($-g\nabla_h^2\eta$), i.e., the right-hand side terms in Eq. (15) (e.g., Errico, 1980; Gill, 1982; Klein et al., 2008; Molemaker et al., 2010; modified from Chavanne et al., 2010 because variance estimate does not require absolute value):

$$\kappa = \frac{\left\langle \left(f_c\zeta - g\nabla_h^2\eta\right)^2 \right\rangle}{2\left[\left\langle \left(f_c\zeta\right)^2 \right\rangle + \left\langle \left(g\nabla_h^2\eta\right)^2 \right\rangle\right]}, \tag{19}$$

where $\kappa \to 0$ and $\kappa \to 1$ denote the dominance of geostrophy and ageostrophy, respectively (according to Cauchy's inequality), and the angle bracket ($\langle\cdot\rangle$) indicates the expectation value of a variable. Note that κ may not be valid for strong vortices, such as centrifugal force divergence (e.g., Molemaker et al., 2010).

The degree of geostrophic imbalance (χ) is defined as the normalized magnitude of the mismatch between the Coriolis force and pressure gradients:

$$\chi = \frac{-\left\langle \left(f_c\zeta\right)^2 \right\rangle + \left\langle \left(g\nabla_h^2\eta\right)^2 \right\rangle}{\left\langle \left(f_c\zeta\right)^2 \right\rangle + \left\langle \left(g\nabla_h^2\eta\right)^2 \right\rangle}, \tag{20}$$

where $\chi \to -1$ and $\chi \to 1$ denote the dominance of the Coriolis force ($f_c\zeta$) and pressure gradients ($g\nabla_h^2\eta$), respectively.

Both the degree of geostrophy and the degree of geostrophic imbalance can be presented in the physical space (e.g., time domain and spatial domain) or in the spectral domain (e.g., frequency domain and wavenumber domain) as well as a distance from the shore or a water depth (Eqs. (1), (2), (9), and (10)), to substantiate the interactions between oceanographic processes and coastal boundaries (e.g., the coastal transition zone, delineation of near-inertial motions and pure inertial motions in a coastal region, and the effective cross-shore region of coastally trapped waves).

A threshold of the degree of geostrophy (κ_1) can be chosen to delineate the geostrophic (σ_g) and ageostrophic (σ_{ag}) frequency bands:

$$\sigma = \begin{cases} \sigma_g & \text{if } \kappa \leq \kappa_1 \\ \sigma_{ag} & \text{if } \kappa > \kappa_1 \end{cases}. \tag{21}$$

An additional threshold (κ_2) of the degree of agoestrophy can be applied to hold more mismatches between the two terms depending on the signal-to-noise ratio of the observed data and numerical model outputs. Similarly, a threshold of the degree of geostrophic imbalance can be applicable.

3.2.3. Variance distribution

The fractions of the cumulative variance in the total surface currents (α), geostrophic currents (β), and ageostrophic surface currents (γ) are estimated as follows,

$$\alpha(\sigma) = \frac{1}{S}\int_{|\sigma_0|}^{|\sigma|} S_{\mathbf{u}}(\varsigma)\mathrm{d}\varsigma, \tag{22}$$

$$\beta(\sigma) = \frac{1}{S}\int_{|\sigma_0|}^{|\sigma|} S_{\mathbf{u}_g}(\varsigma)\mathrm{d}\varsigma, \tag{23}$$

$$\gamma(\sigma) = \frac{1}{S}\int_{|\sigma_0|}^{|\sigma|} S_{\mathbf{u}_{ag}}(\varsigma)\mathrm{d}\varsigma, \tag{24}$$

where σ_0 denotes the lowest frequency. $S_{\mathbf{u}_g}$ and $S_{\mathbf{u}_{ag}}$ are estimated from geostrophic currents and ageostrophic currents, respectively, and

$$S = \int S_{\mathbf{u}}(\varsigma)\mathrm{d}\varsigma. \tag{25}$$

The cumulative variance can highlight the variance in narrow frequency bands (e.g., diurnal and semi-diurnal frequency bands) with step functions and the variance at high-frequency, which may not be easily visualized in the regular variance presentation with energy spectra.

4. Results

4.1. Spectral content of currents and SSHs

We present the spectral content of currents and SSHs in three ways to visualize signals embedded in the data and to rationalize partitioning of the total variance into variance in the distinct frequency and wavenumber bands: variance in the (1) frequency domain and cross-shore distance (Fig. 2), (2) frequency and cross-shore wavenumber domains (Fig. 3), and (3) frequency and azimuthally averaged horizontal wavenumber domains (Fig. 4) (see Section 3.1 for more detailed formulations). Furthermore, the energy spectra in frequency and azimuthally averaged horizontal wavenumber domains can be used as a tool to interpret geostrophy and ageostrophy along with the dispersion relationship of internal waves or IGWs under several primary modes (Fig. 4 and Appendix A) (e.g., Klein et al., 2009; Rocha et al., 2016a).

In the frequency domain and cross-shore distance (Eqs. (1) and (2); Fig. 2), the dominant variance appears in the low-frequency band ($|\sigma| \leq 0.2$ cpd), near-inertial frequency band ($|\sigma - f_c| \leq 0.1$ cpd, where f_c denotes the local Coriolis frequency) and tidal frequencies (K_1 and M_2) (Fig. 2a, b, and d). The low-frequency variance was enhanced near the coast ($0 < x \leq 30$ km), which is associated with wind-driven geostrophic currents near the coast and subinertial alongshore SSH variability, such as coastally trapped waves and regional- and basin-scale wind setups (Fig. 2). Based on observations of the near-inertial surface currents in the study domain (e.g., Kim et al., 2011; Kim and Kosro, 2013; Kim et al., 2014, 2015b), the variance in the near-inertial currents is enhanced offshore, decreases shoreward, and disappears near the coast ($0 < x \leq 30$ km) due to restricted circular inertial motions associated with the coastline and bottom topography (e.g., Kim et al., 2011) (Fig. 2a and b). The variance of the AVISO-derived SSHAs and ROMS-simulated SSHs has a similar order of magnitude in the frequency ranges that both time series can resolve (Fig. 2c and e). The variance distribution in the cross-shore direction and frequency domain is nearly equivalent (Fig. 2c and e).

In the frequency and cross-shore wavenumber domains (Eqs. (3) and (4); Fig. 3), the dominant variance in the ROMS-simulated surface currents in D1 is saturated in three primary frequency bands (e.g., low-frequency, near-inertial, and semi-diurnal frequency bands) and is spread in the wavenumber domain (see Soh and Kim, 2018 for another example of the kinetic energy spectra of surface currents in a coastal region) (Fig. 3a). On the contrary, the dominant variance in the ROMS-simulated SSHs appears in three slightly different frequency bands (e.g., low-frequency, diurnal, and semi-diurnal frequency bands) because SSHs do not contain near-inertial motions and are coherent with surface tides. Moreover, the variance of the ROMS-simulated SSHs appears as the enhanced and vertically mirrored patterns at the super-inertial frequency with a linear or parabolic increase with frequency (Fig. 3b). This feature can be explained with the linear dispersion curves of low mode IGWs as the SSH signatures of the IGW continuum (e.g., Savage et al., 2017a,b). Although Sasaki et al. (2014) reported that the daily averaged submesoscale currents in the open ocean contain primarily geostrophic currents and negligible ageostrophic components (see Supplementary Information Figure 3 in Sasaki et al., 2014 for more details), the observed surface currents in both open ocean and coastal regions have significant variance in the near-inertial and tidal frequency bands (e.g., Elipot and Lumpkin, 2008; Kim et al., 2011; Kim and Kosro, 2013).

In the azimuthally averaged energy spectra (Eqs. (5) and (6); Fig. 4), the HFR-derived and ROMS-simulated surface currents in D2 (a green box in Fig. 1b) show common features of insignificant IGWs, variance in low-frequency and low-wavenumber, and near-inertial variance having longer than 50 km spatial scale (Fig. 4a and b). On the contrary, the ROMS-simulated surface currents have more meaningful signals in the spatial scale shorter than 10 km than the HFR-derived surface currents do, which appears as the variance in most frequencies (e.g., low frequency to super-inertial frequency) (Fig. 4a and b). The smoothed and insignificant variance of the HFR-derived surface currents in that spatial scale supports the effective spatial resolution of 20 to 30 km (Section 2.3). Although the order of magnitude of variance of the ROMS-simulated surface currents and SSHs may be different, they have consistent variance distribution ranging from 5 to 10 km spatial scales (Fig. 4b and c). The azimuthally averaged energy spectra of the ROMS-simulated surface currents sampled in D2 and D3 are nearly identical, including invisible features of IGWs except that the variance in the surface currents in D2 is enhanced at low frequencies and low wavenumbers (not shown). Similarly, the azimuthally averaged energy spectra of the MITgcm-simulated surface currents sampled in D2 and D3 do not show the modal dispersion relationship of IGWs (not shown). This difference may not be consistent with other regional circulation studies using MITgcm llc4320 products (e.g., Torres et al., 2018; Mazloff et al., 2020) and can be interpreted that IGWs may be dissipated within the coastal domain due to bathymetry and shoreline or IGWs may not be simulated as much as they should be in this region.

The hourly HFR-derived surface currents may not have features of IGWs at high wavenumber because a series of data processing to obtain hourly surface current maps (e.g., temporal averaging and spatial mapping) may not maintain IGWs: (1) A single radial velocity map is hourly averaged from 5 to 7 radial velocity maps within an hour; (2) Multiple hourly radial velocity maps from independent sites are combined into hourly vector surface currents (e.g., Kim et al., 2008; Kim, 2010). However, spatial smoothing on IGWs can be minimal because OI mapping is designed to reduce spatial smoothing by applying an exponentially decaying spatial function. Thus, we conclude that the IGWs in this region are not observed in the HFR-derived surface currents.

4.2. Delineation of geostrophy and ageostrophy

The cross-shore time series of SSHs and the geostrophic and ageostrophic currents in D1 are shown in Fig. 5a to e. The ROMS-simulated ageostrophic surface currents contain the components associated with tides, near-inertial motions, wind-incoherent low-frequency components, and noise. Specifically, the ageostrophic surface currents coherent with barotropic tides and near-inertial motions appear as the nearly in-phased currents, i.e., the vertical line features in Fig. 5c and e. The low-frequency ageostrophic surface currents are related to long periodic tidal motions (e.g., spring–neap tide and fortnightly tide), and their reduced cross-shore variations near the coast are visible as a result of coastal boundary effects (e.g., bottom bathymetry and shoreline) (Fig. 5c and e).

The energy spectra of the ROMS-simulated total surface currents appear as red spectra in the wavenumber domain (Fig. 6a) and frequency domain (Fig. 6b), including the variance in the low-frequency and near-inertial frequency bands and at tidal frequencies and their harmonics. A comparison of the variance in the ROMS-simulated and MITgcm-simulated surface currents yields the following findings:

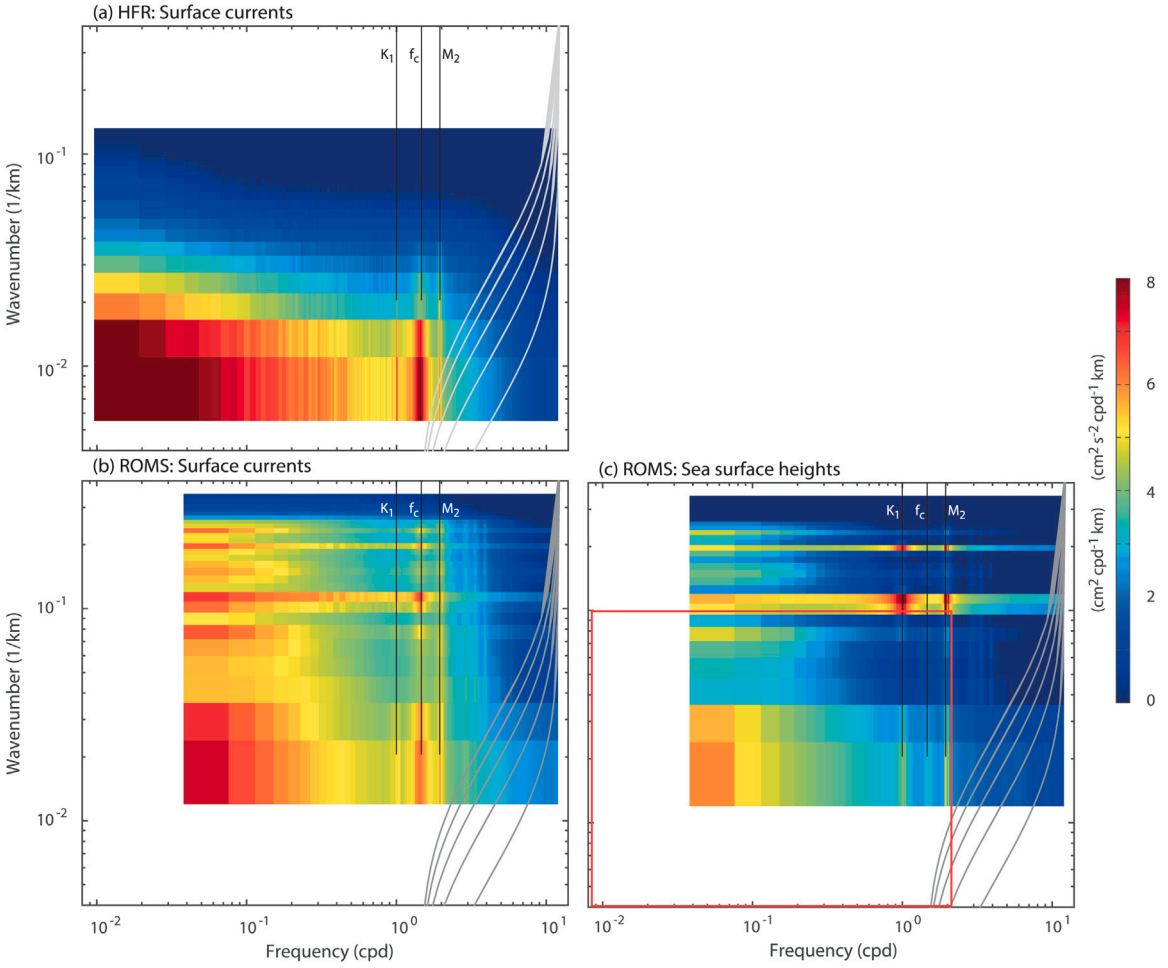

Fig. 4. Azimuthally averaged wavenumber–frequency-domain energy spectra of the HFR-derived (a) surface currents ($cm^2\ s^{-2}\ cpd^{-1}\ km$) in D2 (a green box in Fig. 1b) and ROMS-simulated (b) surface currents ($cm^2\ s^{-2}\ cpd^{-1}\ km$) and (d) SSHs ($cm^2\ cpd^{-1}\ km$) in D2 (a light green box in Fig. 1b). The dispersion relationship of IGWs at the first five vertical modes is marked with gray curves. A red box in Fig. 4c corresponds to the ranges of the wavenumber and frequency in Fig. 3.

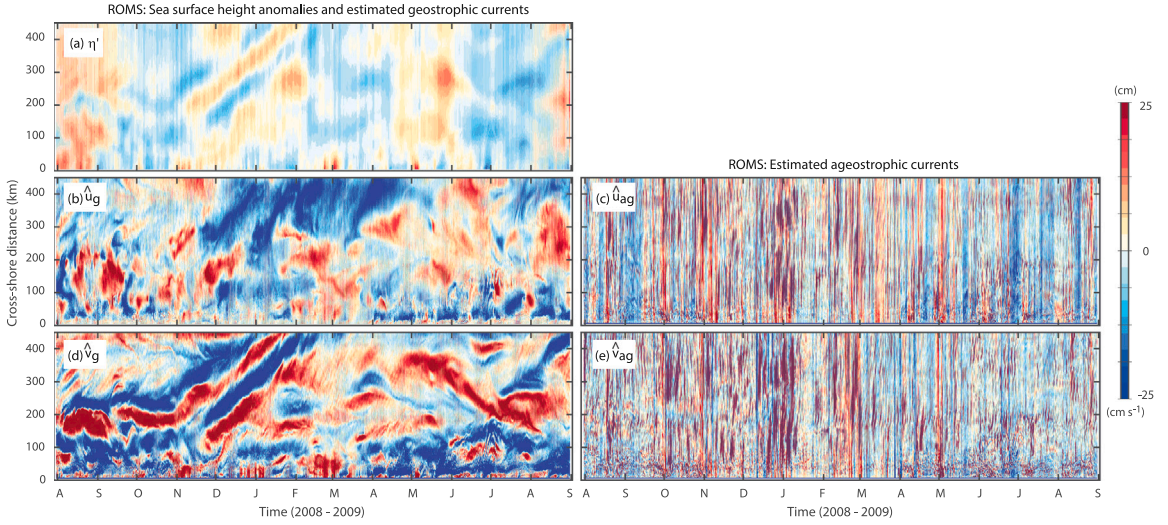

Fig. 5. Hourly cross-shore time series of ROMS-simulated (a) detided SSHs (η'; cm), [(b) and (d)] geostrophic currents (u_g and v_g; $cm\ s^{-1}$), [(c) and (e)] ageostrophic currents (u_{ag} and v_{ag}; $cm\ s^{-1}$) along the NH line (D1).

(1) the ROMS-simulated surface currents have more variance than the MITgcm-simulated surface currents at low wavenumbers and low frequencies; (2) the MITgcm-simulated surface currents have more variance than the ROMS-simulated surface currents at the M_2 frequency and its higher harmonic frequencies (M_4 and M_6), which follows the Garrett–Munk (GM) spectrum (e.g., Munk, 1981) (Fig. 6a and b). These differences in spectral content can be explained as follows: (1) the bottom boundary layer over the continental shelves can be more

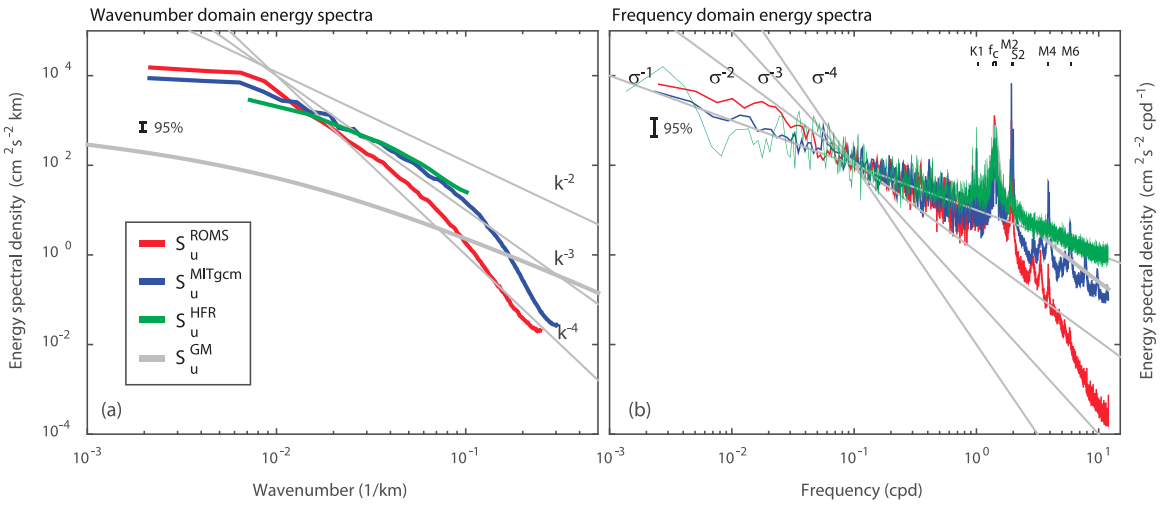

Fig. 6. Energy spectra of the ROMS-simulated (S_u^{ROMS}), MITgcm-simulated (S_u^{MITgcm}), and HFR-derived (S_u^{HFR}) surface currents along the NH line (D1) in the (a) wavenumber domain and (b) frequency domain. Gray auxiliary lines of k^{-2}, k^{-3}, and k^{-4} spectral slopes and σ^{-1}, σ^{-2}, σ^{-3}, and σ^{-4} spectral slopes and the scaled Garrett–Munk (GM) spectrum of currents (S_u^{GM}) are overlaid. Individual error bars are marked with 95% confidence intervals.

physically implemented with the σ-coordinate model (ROMS) than the z-coordinate model (MITgcm) (Allen et al., 1995; Allen and Newberger, 1996) due to the full step or partial step bottom bathymetry over the continental shelves in the z-coordinate model (e.g., Adcroft et al., 1997), which have potential of artifacts or enhance variance in the simulations of the wind-driven coastal upwelling and down-welling and internal waves/tides near the continental shelves; (2) the regional model misses the propagation of remotely-generated internal tides, and the remotely-generated tides in the global model are the source of IGW spectrum filling at high wavenumbers and frequencies (e.g., Ponte and Cornuelle, 2013).

Examples of the ROMS-simulated normalized vorticity ($\xi = \zeta/f_c$) and surface currents in D5 are presented with their total, geostrophic, and ageostrophic components (Fig. 7).

Geostrophic currents and ageostrophic currents (Eqs. (11), (12), (13), and (14)) show dominant variances at length scales longer and shorter than 15 km, respectively (Figs. 8a and B.1a). However, simple spatial derivatives of SSHs may not be valid for high-wavenumber and high-frequency bands because (1) the geostrophic balance is not valid in these wavenumber and frequency bands, and (2) the variances of geostrophic and ageostrophic currents appear to be higher than the variance of the total surface currents (Fig. 8b). Assuming that a series of the SSH maps (with spatial resolutions of less than 1 km and temporal resolutions of days to weeks) obtained from the SWOT mission are available, the spatial derivatives of the SSHs using geostrophic balance and band-pass filtering of their wavenumber-domain energy spectrum is the only way to delineate the geostrophic and ageostrophic currents. Thus, the wavenumber-domain energy spectra of the ROMS-simulated and MITgcm-simulated surface currents in Fig. 8a and c provide examples of when the geostrophic currents and internal tides (M_2) are dominant in the sampled SSHs, respectively. The variance in the currents estimated from the geostrophic balance may be higher than the variance in the total currents in most of the wavenumbers (Fig. 8c) and high frequency ($\sigma > M_4$) (Fig. 8d), which should serve as a cautionary reminder regarding the blind analysis of a series of high-resolution SSH maps. Because simple mathematical differentiation of the given SSHs may yield physically meaningless artifacts in the estimates of geostrophic and ageostrophic currents, particularly in the coastal regions.

The degree of geostrophy and the degree of geostrophic imbalance in the frequency domain show that the geostrophic balance is valid for a period of longer than 3 to 10 days (Fig. 9a and b). To interpret the degree of geostrophy, the threshold degrees of geostrophy in the frequency domain ($\kappa_1 = 0.1$ and $\kappa_2 = 0.2$) of the ROMS-simulated surface currents and corresponding threshold frequencies (σ_1 and σ_2) are marked in Fig. 9a and b (red and orange curves) (see Fig. C.1a for the same threshold degrees of geostrophy of the ROMS-simulated normalized vorticity and corresponding threshold frequencies; red and black curves). The frequency bands with proper geostrophic balances can be identified using the degree of geostrophy [$\kappa = \kappa(\sigma, x)$]. The threshold frequencies (σ_1 and σ_2), which appear in the sub-diurnal frequency band, reach a maximum approximately 80 km from the coast and decrease in the offshore and onshore directions. This is because (1) the influence of the coastal geostrophic balance against the coast is dominant near the coast, and (2) the frictional balance and boundary-free geostrophic balance are the ruling factors in the onshore and offshore regions, respectively (Fig. 9a). Although the chosen threshold value (κ) is less than 0.1, the cross-shore structure at the threshold frequency varies slightly within the error bar. The degree of geostrophy highlights the contribution of the semidiurnal variance (M_2); however, it may not adequately capture the influence of near-inertial variance (Fig. 9a) because the near-inertial motions can be considered as unbalanced wave motions and balanced near-inertial advection.

Considering the individual terms in the degree of geostrophic imbalance (χ), the Coriolis term becomes significant in the near-inertial frequency band ($|f_c\zeta| \gg |g\nabla_h^2\eta|$) and has wide peaks offshore. Moreover, the pressure gradients become dominant in the superinertial frequency band ($|f_c\zeta| \ll |g\nabla_h^2\eta|$) (Fig. 9b). Thus, the ageostrophic currents in the superdiurnal frequency band can be divided into two components of near-inertial variance-dominant ageostrophic currents and pressure gradient-dominant ageostrophic currents.

The degree of geostrophy and the degree of geostrophic imbalance in the wavenumber domain show that the geostrophic balance is valid for a length scale longer than approximately 50 km (Fig. 9d and e). Similar to the previous analysis of indicators in the frequency domain, the threshold degree of geostrophic imbalance in the wavenumber domain ($\chi_1 = 0.1$ and $\chi_2 = 0.2$) of the ROMS-simulated surface currents and corresponding threshold wavenumbers (k_1 and k_2) are marked in Fig. 9d and e (red and orange curves). These exhibit a transition close to 50 to 100 km from the coast and at a water depth of approximately 250 m where (1) the influence of the continental shelf and slope on the coastal circulation becomes dominant and (2) mesoscale and submesoscale processes lead to mixing of shelf/slope waters and open ocean waters, for example, in a coastal transition zone (e.g., Kundu et al., 1983; Brink et al., 1991; Brink and Cowles, 1991; Springer et al., 2009).

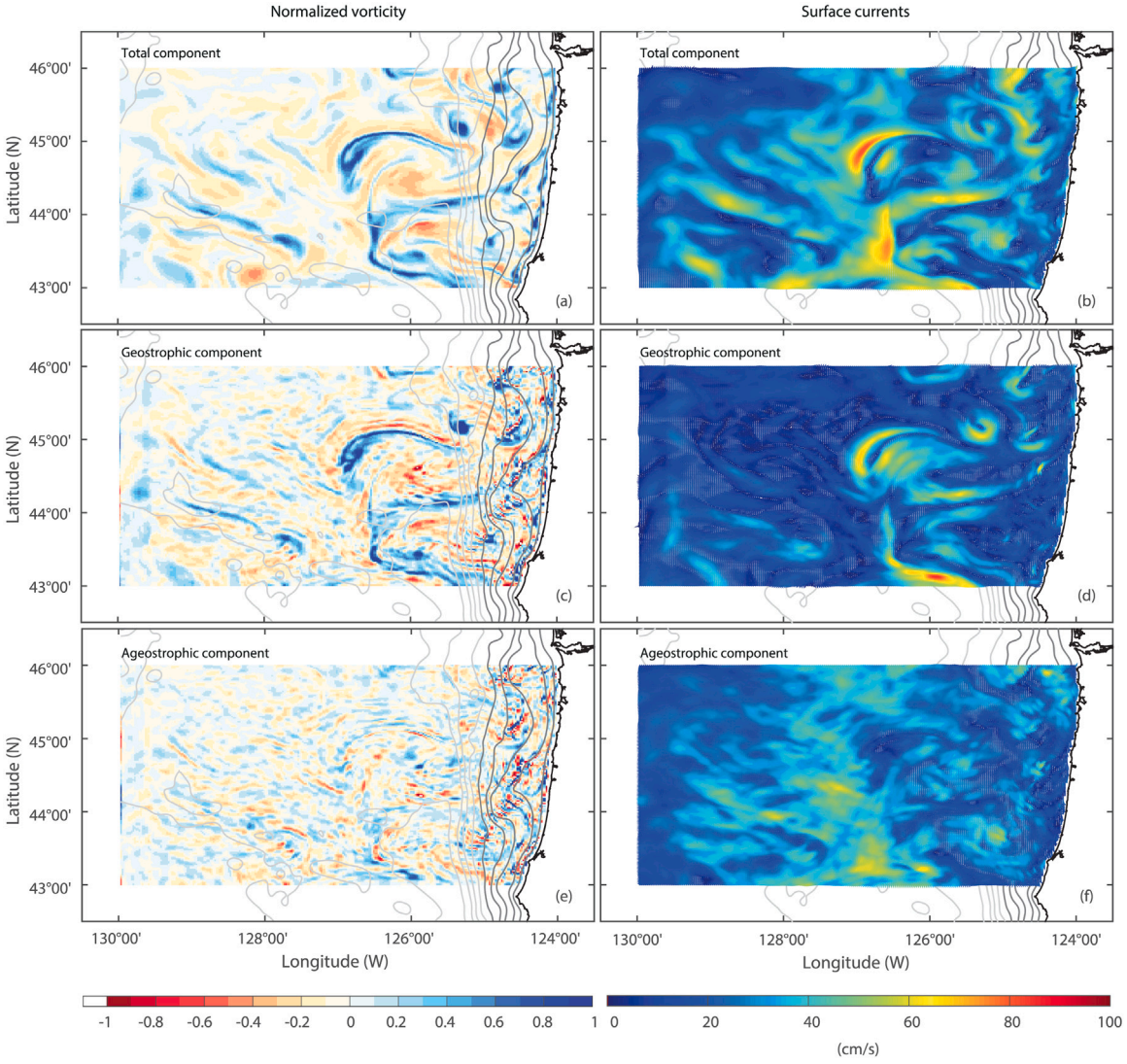

Fig. 7. Examples of the ROMS-simulated [(a), (c), and (e)] normalized vorticity [$\xi = \zeta/f_c = (\partial v/\partial x - \partial u/\partial y)/f_c$] and [(b), (d), and (f)] surface currents ($\mathbf{u}$) in D5 presented with their [(a) and (b)] total component ($\mathbf{u}$ and ξ), [(c) and (d)] geostrophic component ($\mathbf{u}_g$ and ξ_g), and [(e) and (f)] ageostrophic component ($\mathbf{u}_{ag}$ and ξ_{ag}). Note that the magnitude of surface currents are color-coded.

4.3. Variance distribution

The variances of the geostrophic, ageostrophic, and total current components are examined using the quantities averaged in the cross-shore direction, and this value is presented as a function of frequency (Fig. 9g). In particular, the fractions of the variance in the four primary frequency bands are categorized as low ($0 < |\sigma_L| \leq 0.36$ cpd), diurnal (0.95 cpd $\leq |\sigma_D| \leq 1.05$ cpd), near-inertial (1.21 cpd $\leq |\sigma_{NI}| \leq 1.57$ cpd), or semi-diurnal (1.90 cpd $\leq |\sigma_S| \leq 2.05$ cpd) frequency bands relative to the variance in the total currents shown in Table 1 (Fig. 9g). As a significant component of the ageostrophic surface currents, the near-inertial surface currents account for 18% of the total variance and approximately 40% of the ageostrophic variance. The low-frequency currents are not always geostrophically balanced because of low-frequency components associated with ageostrophic currents.

Table 1
Fraction of variance of the ROMS-simulated total surface currents ($\mathbf{u}$) and Rossby number (ξ), geostrophic currents ($\mathbf{u}_g$) and Rossby number (ξ_g), and ageostrophic surface currents ($\mathbf{u}_{ag}$) and Rossby number (ξ_{ag}) in the primary frequency bands: low-frequency (0 cpd $< |\sigma_L| \leq 0.36$ cpd), diurnal (0.95 cpd $\leq |\sigma_D| \leq 1.05$ cpd), near-inertial (1.21 cpd $\leq |\sigma_{NI}| \leq 1.57$ cpd), semi-diurnal (1.90 cpd $\leq |\sigma_S| \leq 2.05$ cpd) frequency bands, the rest of frequencies ($|\sigma_E|$), and the entire frequencies (0 cpd $< |\sigma_A| \leq 12$ cpd).

	σ_L	σ_D	σ_{NI}	σ_S	σ_E	σ_A
$\langle \mathbf{u}^2 \rangle$	55.8	1.5	18.4	11.9	12.4	100.0
$\langle \mathbf{u}_g^2 \rangle$	44.2	0.5	0.3	5.2	4.0	54.2
$\langle \mathbf{u}_{ag}^2 \rangle$	11.6	1.0	18.1	6.7	8.4	45.8
$\langle \xi^2 \rangle$	73.4	1.4	5.2	4.5	15.5	100.0
$\langle \xi_g^2 \rangle$	73.3	0.1	0.1	0.1	7.9	81.5
$\langle \xi_{ag}^2 \rangle$	0.1	1.3	5.1	4.4	7.6	18.5

5. Discussion

5.1. Spatial homogeneity and temporal stationarity of the data in a coastal region

Oceanographic physical processes are typically considered spatially homogeneous and temporally stationary in the open ocean, which indicates that (1) the sampled data in the finite temporal and spatial domains are repeated in the individual domains infinitely, and (2) the sample data covariances are only a function of spatial lags or temporal lags (or both) (e.g., Emery and Thomson, 1997; Kim, 2010). However, the physical processes near physical boundaries (e.g., the coast or bottom bathymetry) or dynamical boundaries (e.g., fronts and eddies) may be neither homogeneous nor stationary.

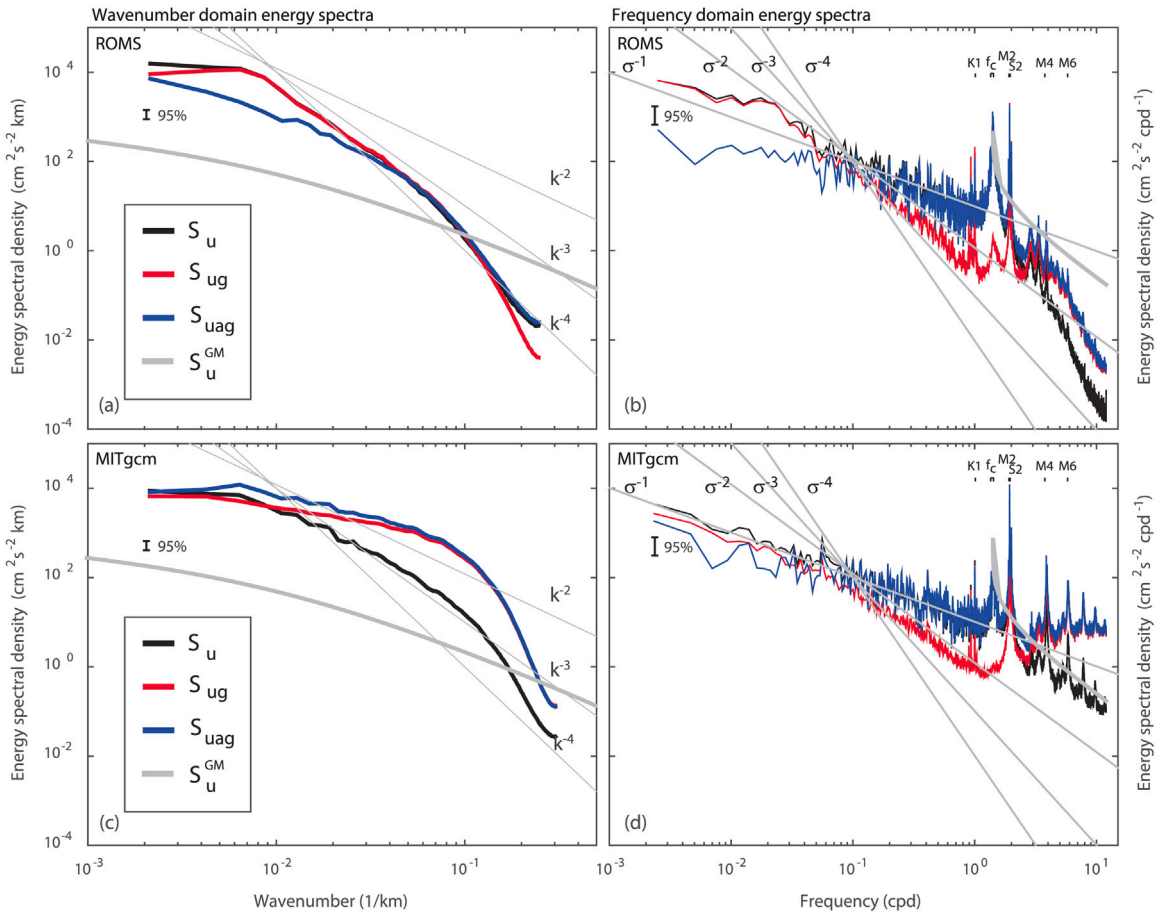

Fig. 8. [(a) and (b)] (c) Energy spectra of the ROMS-simulated total surface currents ($S_{\mathbf{u}}$), geostrophic currents ($S_{\mathbf{u}_g}$), ageostrophic currents ($S_{\mathbf{u}_{ag}}$) on the NH line (D1) in the (a) wavenumber domain and (b) frequency domain. [(c) and (d)] Energy spectra of the MITgcm-simulated surface currents ($S_{\mathbf{u}}$), geostrophic currents ($S_{\mathbf{u}_g}$), ageostrophic currents ($S_{\mathbf{u}_{ag}}$) along the NH line (D1) in the (a) wavenumber domain and (b) frequency domain. Gray auxiliary lines of k^{-2}, k^{-3}, and k^{-4} spectral slopes and σ^{-1}, σ^{-2}, σ^{-3}, and σ^{-4} spectral slopes and the scaled Garrett–Munk (GM) spectrum of currents ($S_{\mathbf{u}}^{\mathrm{GM}}$) are overlaid. Individual error bars are marked with 95% confidence intervals.

In particular, both observed and simulated surface currents and SSHs in this paper may not have spatial homogeneity and temporal stationarity. Thus, we describe the detailed justification of how we can assume our sampled data to be locally homogeneous in space and stationary in time in the estimates of the energy spectra by adopting a similar analysis used in the estimates of spatial covariance (e.g., Yoo et al., 2017). Firstly, the spatial homogeneity has been evaluated with how consistently the spatial covariances and wavenumber-domain energy spectra are estimated when they are computed with the data (e.g., surface current components and SSHs), sampled from different domain sizes as a function of the radius from the center of the domain of interest. As we increase the domain's size, the sampled data can have less spatial homogeneity as a result of enhanced spatial variability. In this paper, the shape of the estimated wavenumber-domain energy spectra is nearly identical when the radius is in a range of 10 km to 25 km. The spatial homogeneity of surface currents was separately evaluated with current components (u and v) because the surface current field can be anisotropic. Likewise, the temporal stationarity has been investigated with the estimates of temporal covariances and frequency-domain energy spectra from the data with different time window sizes as a function of the data length. The shape of the estimated frequency-domain energy spectra is consistently maintained when more than one-half of a year of data is used. This can also be discussed based on the influence of the number of realizations: the greater the number of realizations, the greater the number of robust estimates in the energy spectra, possibly having less statistical noise. For instance, the estimated energy spectra under more realizations are closer to a constant value of the energy spectrum, and the error bar of the energy spectra becomes narrow, as can be found in Priestley (1981) and closely relevant to the sensitivity test of spectral estimates. As mentioned earlier, the jackknife method has been used to estimate confidence intervals of the statistical estimates and to evaluate the convergence of the estimates in this paper (e.g., Emery and Thomson, 1997; Kim et al., 2009).

5.2. Reconstruction of submesoscale coastal currents using high-resolution SSHs

Recent studies have examined whether open ocean currents at submesoscale are predominantly geostrophic flows. Sasaki et al. (2014) reported that submesoscale currents in the open ocean are considered geostrophically balanced without including tidal forcing in their simulation, which is essential to obtain a realistic IGW field. Qiu et al. (2018) found evidence for seasonality in unbalanced (IGWs) motions as well as in balanced (submesoscale turbulence) surface currents that were out of phase, with unbalanced dominating in summer and balanced dominating in winter in most of the open ocean, resulting in seasonality in the transition scale, based on the MITgcm llc4320 global simulation as an extension of the results of Sasaki et al. (2014). However, the open ocean current observations find somewhat less seasonality (e.g., Rocha et al., 2016a) and significant seasonality (e.g., Callies et al., 2015) in the transition scale between predominantly geostrophic flows to predominantly ageostrophic flows. Likewise, coastal currents at submesoscale have predominantly geostrophic flows and predominantly ageostrophic flows. As a follow-up to the SWOT mission (e.g.,

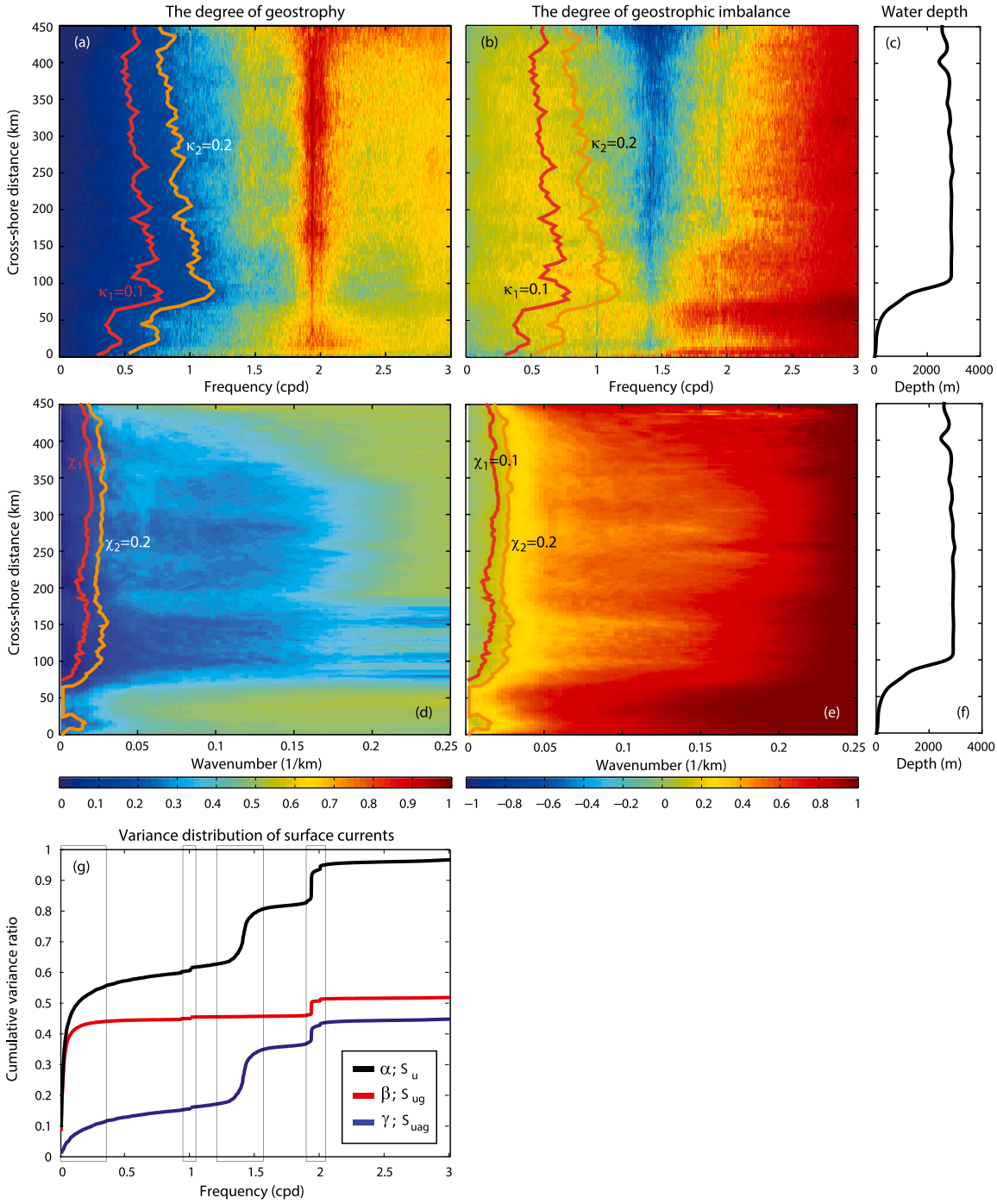

Fig. 9. (a) and (b): The degree of geostrophy [geostrophic ($\kappa \to 0$) and ageostrophic ($\kappa \to 1$) conditions] and the degree of geostrophic imbalance [dominance of the Coriolis force ($\chi \to -1$) and pressure gradients ($\chi \to 1$)], estimated from ROMS-simulated surface currents in D4 are presented as a function of frequency and cross-shore distance. Two threshold values of the degree of geostrophy in the frequency domain ($\kappa_1 = 0.1$ and $\kappa_2 = 0.2$) are marked with red and orange colors in Fig. 9a and b (see Fig. C.1a for comparison). (c) and (f): Cross-shore depth profile as a function distance from the coast. (d) and (e): The degree of geostrophy and the degree of geostrophic imbalance, estimated from ROMS-simulated surface currents in D5 are presented as a function of wavenumber and cross-shore distance. Two threshold values of the degree of geostrophic imbalance in the wavenumber domain ($\chi_1 = 0.1$ and $\chi_2 = 0.2$) are marked with red and orange colors in Fig. 9d and e. (g) A fractional cumulative variance of the total surface currents ($S_{\mathbf{u}}$; α in Eq. (22)), geostrophic currents ($S_{\mathbf{u}_g}$; β in Eq. (23)), and ageostrophic surface currents ($S_{\mathbf{u}_{ag}}$; γ in Eq. (24)) [see Table 1 for more details]. A magnified view between 0 cpd and 3 cpd is only presented. Gray boxes indicate primary frequency bands of low-frequency (0 cpd $< |\sigma_L| \leq$ 0.36 cpd), diurnal (0.95 cpd $\leq |\sigma_D| \leq$ 1.05 cpd), near-inertial (1.21 cpd $\leq |\sigma_{NI}| \leq$ 1.57 cpd), and semi-diurnal (1.90 cpd $\leq |\sigma_S| \leq$ 2.05 cpd) frequency bands.

Ubelmann et al., 2014, 2015; Gaultier et al., 2016; Wang et al., 2018), the conversion from high-resolution SSHs to submesoscale currents requires careful analysis. Gaultier et al. (2016) and Wang et al. (2018) reported that the retrieval of current fields under SWOT missions could be limited to spatial scales of longer than 70 to 85 km. Estimation of currents from satellite SSH observations may require in-situ observations for calibration, evaluation, and complementary information, such as HFR-derived surface currents, to complement the circulation information using constructive data integration to resolve the entire submesoscale currents. The statistical relationships, such as the spatial covariance between stream function (or velocity potential) and

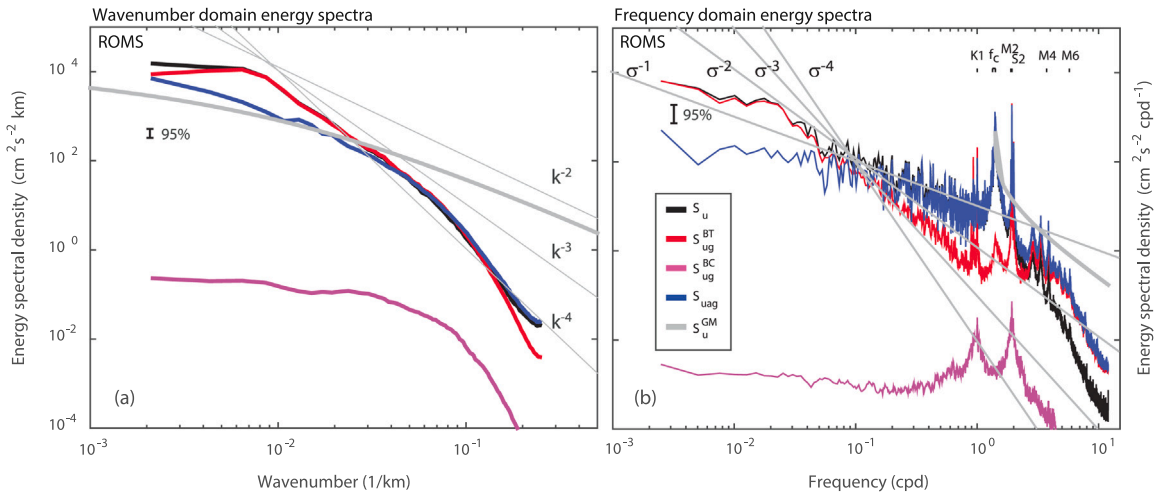

Fig. B.1. Wavenumber-domain energy spectra and frequency-domain energy spectra of the ROMS-simulated total surface currents ($S_{\mathbf{u}}$), geostrophic currents for barotropic components ($S_{\mathbf{u}_g}^{\mathrm{BT}}$) and baroclinic components ($S_{\mathbf{u}_g}^{\mathrm{BC}}$), ageostrophic surface currents ($S_{\mathbf{u}_{ag}}$) along the NH line (D1) are presented. Gray auxiliary lines of k^{-2}, k^{-3}, and k^{-4} spectral slopes and Garrett–Munk (GM) spectra of currents ($S_{\mathbf{u}}^{\mathrm{GM}}$) are marked. Gray auxiliary lines of σ^{-1}, σ^{-2}, σ^{-3}, and σ^{-4} spectral slopes and GM spectra of currents ($S_{\mathbf{u}}^{\mathrm{GM}}$) are marked. Individual error bars are marked with 95% confidence intervals.

currents, can be applied to estimate an SSH proxy and evaluate the reconstruction capability (e.g., Kim, 2010; Firing et al., 2014). Beyond data integration, idealized theoretical assumptions and dynamical frameworks, such as surface quasi-geostrophic (SQG) theory, effective SQG theory (e.g., Qiu et al., 2016; Lapeyre and Klein, 2006; Ponte and Klein, 2013) and data assimilation techniques (e.g., Carrier et al., 2016 and John Wilkin's efforts at Rutgers University], can be applied to completely resolve entire submesoscale currents. In this case, implementing surface gravity waves, internal waves, tides, and submesoscale processes, including baroclinic instability and strain-induced frontogenesis, can be challenging.

5.3. Ageostrophy of coastal circulation

The ageostrophic components, i.e., residuals in the geostrophic balance (Eqs. (11) and (12)), in coastal regions can be associated with wind stress divergence, barotropic and baroclinic tides, asymmetric pressure gradients, near-inertial surface (or internal) waves, and IGWs. For instance, the inertial currents have pure-inertial motions offshore and are modified into near-inertial motions within one or two internal Rossby radii of deformation from the coast because they are effectively reduced near the coast due to the influence of coastal boundaries (e.g., Pettigrew, 1981; Kim and Kosro, 2013; Kim et al., 2011, 2014, 2015b; Shearman, 2005). The decay of the elliptical near-inertial currents in geostrophic and ageostrophic flows can be easily described in the context of the contributions of geostrophy and ageostrophy. The vertical components of ageostrophic currents are associated with the internal motions or vertical displacement of the thermocline. The estimated divergence of surface currents, i.e., velocity potential-derived vertical currents, should be carefully addressed regarding their relevance to submesoscale vertical currents.

5.4. General and regional implications

The analysis and findings in this paper can provide lessons in the delineation of geostrophy and ageostrophy as general and site-specific implications. The ocean circulation and physical ocean processes off the Oregon coast include wind-driven coastal upwelling and downwelling on a straight coastline as a part of air–sea–land interactions, surface and subsurface near-inertial motions, and barotropic and baroclinic tides. The simple geometry of coastline and complex oceanographic conditions allow us to generalize (1) the transition of these physical processes, (2) the contribution of geostrophy, and (3) the dominant term in the geostrophic balance as a function of a distance from the coast in the view of extracting meaningful fine-scale ocean processes from SSHs obtained from upcoming satellite missions. On the contrary, as the baroclinic Rossby radius off the Oregon coast is relatively smaller than in other coastal upwelling regions in the Eastern Boundaries (e.g., Peru Current, Benguela Current, Canary Current, and West Australian Current), including southern and central California, regional submesoscale features (e.g., eddies and fronts) appear relatively limited. Thus, the contribution of the ageostrophic components (e.g., submesoscale processes), presented in this paper can be evaluated with observations and numerical model simulations in other coastal upwelling regions. Moreover, artifacts associated with finite spatial differentiation of high-resolution model SSHs should be evaluated with other coastal upwelling regions.

Additionally, in this region, comprehensive data sets are available to evaluate high-resolution satellite SSH observations, such as the concurrent in-situ observations from various platforms at the ocean surface and subsurface (e.g., HFRs, gliders, NH line, moorings, satellite remote sensing, including coastal altimetry) (e.g., Barth et al., 2019), cross-validated numerical model simulations (e.g., ROMS), and data assimilated products (e.g., Kurapov et al., 2017) on the ocean circulation from mesoscale to submesoscale. Thus, it would be an excellent venue to derive the general and regional implications by evaluating the geostrophic and ageostrophic properties in other coastal upwelling regions.

6. Conclusions

We investigate statistical and spectral representations of the high-resolution surface currents and SSHs off the Oregon coast to examine the relative contribution of geostrophy and ageostrophy in coastal ocean currents. We analyze forward numerical simulations based primarily on ROMS and use regional observations of HFR-derived surface currents and altimeter-derived geostrophic currents and a subset of global domain numerical simulations (MITgcm) as secondary references.

The regional submesoscale ageostrophic currents account for up to 50% of the total variance and are primarily associated with near-inertial currents and internal tides. Geostrophy becomes dominant at time scales longer than 3 to 10 days and at spatial scales longer than 50 km, and it shows dependence on the water depth and cross-shore distance, associated with the frictional balance in the nearshore and boundary-free geostrophic balance in the offshore region. The

geostrophic imbalance, as an indicator of the mismatch in the geostrophic balance, shows that the Coriolis term becomes dominant in the near-inertial frequency band and that the pressure gradient term becomes dominant in the super-inertial frequency band. These correspond to the near-inertial motions and high-frequency internal waves/tides, respectively. Estimation of currents from satellite SSH observations can be complemented by other concurrent high-resolution observations, including HFR-derived surface velocities and surface drifter-derived tracks. Additional high-resolution observations and data assimilation techniques that stitch the observations and numerical models together will help resolve submesoscale currents correctly in the perspectives of constructive data integration.

This work will provide a way to better understand how well geostrophy and ageostrophy represent the ocean current field at fine scales in coastal regions and apply to the observations of the sea surface height field at a very high spatial resolution from the upcoming satellite missions.

CRediT authorship contribution statement

Eun Ae Lee: Analysis and interpretation of the data. **Sung Yong Kim:** Conception and design, analysis and interpretation of the data, Drafting the article and revising it critically for important intellectual content.

Declaration of competing interest

The authors declare that they have no known competing financial interests or personal relationships that could have appeared to influence the work reported in this paper.

Acknowledgments

This work is supported by grants through the National Research Foundation (NRF), Ministry of Education, Republic of Korea (NRF-2017R1D1A1B03028285) and Ministry of Science, Information, and Communications Technology (MSIT), Republic of Korea (NRF-2021R1A2C1003317). The altimeter products were produced by SSALTO/DUACS and distributed by Archiving, Validation, and Interpretation of Satellite Oceanographic data (AVISO) with support from the National Centre for Space Studies (CNES). Blended sea level anomaly fields are provided by Oregon State University (OSU), National Oceanic and Atmospheric Administration (NOAA) funded, Cooperative Institute for Oceanographic Satellite Studies (CIOSS). The high-frequency radar-derived surface currents are provided by Prof. P. Michael Kosro at OSU, and the ROM simulations were run by Dr. Alexander Kurapov at OSU (currently at NOAA). The MITgcm llc4320 products were provided by Dr. Dimitris Menemenlis at Jet Propulsion Laboratory (JPL), National Aeronautics and Space Administration (NASA) through the Estimating the Circulation and Climate of the Ocean (ECCO) data portal (available at https://data.nas.nasa.gov/ecco/data.php). All authors approved the version of the manuscript to be published.

Appendix A. Dispersion relationship of the Boussinesq IGWs

The dispersion relationship of the Boussinesq IGWs (e.g., Munk, 1981; Qiu et al., 2018) at the jth vertical mode in the wavenumber and frequency domains is overlaid on the azimuthally averaged energy spectra of the surface currents to visually compare the existence of IGWs in the surface currents:

$$\sigma_j^2 = \frac{\mathsf{N}^2 k_h^2 + f_c^2 m_j^2}{k_h^2 + m_j^2} + \mathbf{U}\cdot\mathbf{k}_h, \tag{A.1}$$

where $\mathbf{U}$ and N denote the background horizontal currents and regional buoyancy frequency (cpd), respectively.

$$m_j H = j\pi, \tag{A.2}$$

where m and H indicate the vertical mode ($j \in \mathcal{Z}$, $j = 1, \ldots, 5$) and the effective water depth (m), respectively. The last term in Eq. (A.1) indicates the frequency shift associated with background horizontal currents, which may yield the non-zero frequency and wavenumber crossings of the dispersion curves.

Appendix B. Barotropic and baroclinic components in the geostrophic currents

The geostrophic currents can be considered as the barotropic (BT) and baroclinic (BC) components,

$$u_g(x,y,z) = u_g^{\mathsf{BT}}(x,y) + u_g^{\mathsf{BC}}(x,y,z) = -\frac{g}{f_c}\frac{\partial \eta(x,y)}{\partial y} - \frac{g}{f_c}\frac{\eta(x,y)}{\rho(x,y,z)}\frac{\partial \rho(x,y,z)}{\partial y}, \tag{B.1}$$

$$v_g(x,y,z) = v_g^{\mathsf{BT}}(x,y) + v_g^{\mathsf{BC}}(x,y,z) = \frac{g}{f_c}\frac{\partial \eta(x,y)}{\partial x} + \frac{g}{f_c}\frac{\eta(x,y)}{\rho(x,y,z)}\frac{\partial \rho(x,y,z)}{\partial x}, \tag{B.2}$$

and the ageostrophic currents are the residual currents that geostrophic currents are removed from the total currents (Eqs. (13) and (14)). The variance of the baroclinic components of the geostrophic currents ($S_{\mathbf{u}_g}^{\mathsf{BC}}$) is relatively small (Fig. B.1).

Appendix C. Geostrophic and ageostrophic Rossby number

The relative vorticity normalized by the local Coriolis frequency (ζ/f_c), i.e., the Rossby number (ξ), can be decomposed into both geostrophic and ageostrophic components,

$$\xi = \frac{\zeta}{f_c} = \frac{\zeta_g + \zeta_{ag}}{f_c} = \xi_g + \xi_{ag}, \tag{C.1}$$

where ζ and f_c denote the vertical component of relative vorticity and local Coriolis frequency, respectively.

The normalized relative vorticity (ξ_g) of the geostrophic currents, geostrophic Rossby number, is given by the Laplacian of the SSHs (Eq. (C.2)):

$$\xi_g = \frac{g}{f_c^2}\left(\frac{\partial^2 \eta}{\partial x^2} + \frac{\partial^2 \eta}{\partial y^2}\right) = \frac{g}{f_c^2}\nabla_h^2 \eta. \tag{C.2}$$

Similarly, although the ageostrophic Rossby number (ξ_{ag}) can be estimated to have the geostrophic Rossby number (Eq. (C.2)) removed from the total Rossby number, it may contain nonphysical signals and noise.

The ageostrophic Rossby number can be identified with (1) the residual Rossby number where κ is less than κ_1 ($\kappa \leq \kappa_1$) in the geostrophic frequency band (σ_g) in Eqs. (19) and (21),

$$\xi_{ag} = \xi - \frac{g}{f_c^2}\nabla_h^2 \eta, \tag{C.3}$$

and (2) the normalized relative vorticity of total currents where κ exceeds κ_1 ($\kappa > \kappa_1$) in the ageostrophy frequency band (σ_{ag}) in Eqs. (19) and (21),

$$\xi_{ag} = \xi. \tag{C.4}$$

Specifically, once two frequency bands are identified from variance distribution of the Rossby number as a function of frequency and cross-shore distance, the time series of the Rossby number can be estimated from the inverse Fourier transformation of the Fourier coefficients of

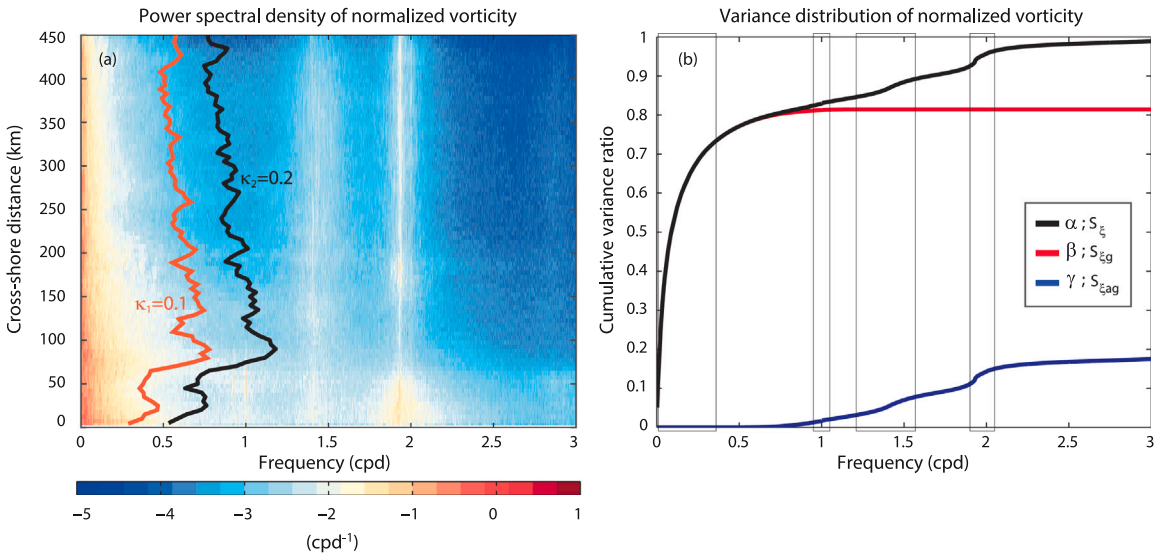

Fig. C.1. (a) Meridionally averaged power spectral density ($\log_{10}$ scale; s^{-2} cpd^{-1}) of ROMS-simulated normalized vorticity [$\xi = \zeta/f_c = (\partial v/\partial x - \partial u/\partial y)/f_c$], estimated from total surface currents in D4 are presented as a function of cross-shore distance. Two threshold values of the degree of geostrophy in the frequency domain ($\kappa_1 = 0.1$ and $\kappa_2 = 0.2$; Fig. 9a and b) are marked as red and black in Fig. C.1a as references. The left-hand-side and right-hand-side of these threshold curves correspond to the frequency bands where geostrophy and ageostrophy are dominant, respectively. (b) A fractional cumulative variance of the total Rossby number (S_ξ; α in Eq. (22)), geostrophic Rossby number (S_{ξ_g}; β in Eq. (23)), and ageostrophic Rossby number ($S_{\xi_{ag}}$; γ in Eq. (24)) [see Table 1 for more details]. A magnified view between 0 cpd and 3 cpd is only presented. Gray boxes indicate primary frequency bands of low-frequency (0 cpd $< |\sigma_L| \leq$ 0.36 cpd), diurnal (0.95 cpd $\leq |\sigma_D| \leq$ 1.05 cpd), near-inertial (1.21 cpd $\leq |\sigma_{NI}| \leq$ 1.57 cpd), and semi-diurnal (1.90 cpd $\leq |\sigma_S| \leq$ 2.05 cpd) frequency bands.

the Rossby number in the finite frequency bands (σ_g and σ_{ag}) using slow Finite Fourier Transform (FFT) (e.g., Kim et al., 2015a):

$$\xi_g(\mathbf{x},t) = \mathrm{Re}\left[\int_{\sigma_g} \hat{\xi}(\mathbf{x},\varsigma)\, e^{i\varsigma t} \mathrm{d}\varsigma\right], \tag{C.5}$$

$$\xi_{ag}(\mathbf{x},t) = \mathrm{Re}\left[\int_{\sigma_{ag}} \hat{\xi}(\mathbf{x},\varsigma)\, e^{i\varsigma t} \mathrm{d}\varsigma\right], \tag{C.6}$$

where $\hat{\xi}$ denotes the Fourier coefficients of the Rossby number.

For instance, the variance distribution of the Rossby number is presented as a function of frequency and cross-shore distance (Fig. C.1a). As the Rossby number and SSHs may not be simply decomposed into their geostrophic and ageostrophic components, the threshold degree of geostrophy (κ_1) is applied (Fig. C.1a). The normalized vorticity contains approximately 80% of the total variance as geostrophic variance (Fig. C.1b and Table 1). The fraction of geostrophy of currents and Rossby number is distributed differently in the frequency domain. For instance, the diurnal, semi-diurnal, and near-inertial variance in Rossby number become insignificant, i.e., low fraction of ageostrophic Rossby number, and the geostrophic Rossby number at low frequency accounts for approximately 70% of the total variance (Fig. C.1b and Table 1).

References

Adcroft, A., Hill, C., Marshall, J., 1997. Representation of topography by shaved cells in a height coordinate ocean model. Mon. Weather Rev. 125 (9), 2293–2315. http://dx.doi.org/10.1175/1520-0493(1997)125<2293:ROTBSC>2.0.CO;2.

Allen, J., Newberger, P., 1996. Downwelling circulation on the Oregon continental shelf. Part I: Response to idealized forcing. J. Phys. Oceanogr. 26, 2011–2035. http://dx.doi.org/10.1175/1520-0485(1996)026<2011:DCOTOC>2.0.CO;2.

Allen, J., Newberger, P., Federiuk, J., 1995. Upwelling circulation on the Oregon continental shelf. Part I: Response to idealized forcing. J. Phys. Oceanogr. 25, 1843–1866. http://dx.doi.org/10.1175/1520-0485(1995)025<1843:UCOTOC>2.0.CO;2.

Alpers, W., 1985. Theory of radar imaging of internal waves. Nature 314, 245–247. http://dx.doi.org/10.1038/314245a0.

Arakawa, A., 1966. Computational design for long-term numerical integration of the equations of fluid motion: Two-dimensional incompressible flow. Part I. J. Comput. Phys. 1 (1), 119–143. http://dx.doi.org/10.1016/0021-9991(66)90015-5.

Archer, M., Schaeffer, A., Keating, S., Roughan, M., Holmes, R., Siegelman, L., 2020. Observations of submesoscale variability and frontal subduction within the mesoscale eddy field of the Tasman Sea. J. Phys. Oceanogr. 50 (5), 1509–1529. http://dx.doi.org/10.1175/JPO-D-19-0131.1.

Ardhuin, F., Aksenov, Y., Benetazzo, A., Bertino, L., Brandt, P., Caubet, E., Chapron, B., Collard, F., Cravatte, S., Delouis, J.-M., et al., 2018. Measuring currents, ice drift, and waves from space: The sea surface kinematics multiscale monitoring (SKIM) concept. Ocean Sci. 14 (3), 337–354. http://dx.doi.org/10.5194/os-14-337-2018.

Ballarotta, M., Ubelmann, C., Pujol, M.-I., Taburet, G., Fournier, F., Legeais, J.-F., Faugère, Y., Delepoulle, A., Chelton, D., Dibarboure, G., et al., 2019. On the resolutions of ocean altimetry maps. Ocean Sci. 15 (4), 1091–1109.

Barth, J.A., Allen, S.E., Dever, E.P., Dewey, R.K., Evans, W., Feely, R.A., Fisher, J.L., Fram, J.P., Hales, B., Ianson, D., et al., 2019. Better regional ocean observing through cross-national cooperation: a case study from the northeast pacific. Front. Mar. Sci. 6, 93. http://dx.doi.org/10.3389/fmars.2019.00093.

Blumen, W., 1967. Energy partition in a barotropic atmosphere. Tellus 19 (2), 174–182. http://dx.doi.org/10.3402/tellusa.v19i2.9763.

Brink, K., Beardsley, R., Niiler, P., Abbott, M., Huyer, A., Ramp, S., Stanton, T., Stuart, D., 1991. Statistical properties of near-surface flow in the California coastal transition zone. J. Geophys. Res. 96 (C8), 14693–14706. http://dx.doi.org/10.1029/91JC01072.

Brink, K., Cowles, T.J., 1991. The coastal transition zone program. J. Geophys. Res. 96 (C8), 14637–14647. http://dx.doi.org/10.1029/91JC01206.

Buckingham, C.E., Garabato, A., Thompson, A., Brannigan, L., Lazar, A., Marshall, D., Nurser, A., Damerell, G., Heywood, K., Belcher, S., 2016. Seasonality of submesoscale flows in the ocean surface boundary layer. Geophys. Res. Lett. 43 (5), 2118–2126. http://dx.doi.org/10.1002/2016GL068009.

Callies, J., Ferrari, R., Klymak, J.M., Gula, J., 2015. Seasonality in submesoscale turbulence. Nature Commun. 6, http://dx.doi.org/10.1038/ncomms7862.

Carrier, M.J., Ngodock, H.E., Muscarella, P., Smith, S., 2016. Impact of assimilating surface velocity observations on the model sea surface height using the NCOM-4DVAR. Mon. Weather Rev. 144 (3), 1051–1068. http://dx.doi.org/10.1175/MWR-D-14-00285.1.

Chapman, D.C., 1987. Application of wind-forced, long, coastal-trapped wave theory along the California coast. J. Geophys. Res. 92 (C2), 1798–1816. http://dx.doi.org/10.1029/JC092iC02p01798.

Chavanne, C., Flament, P., Klein, P., Gurgel, K.-W., 2010. Interactions between a submesoscale anticyclonic vortex and a front. J. Phys. Oceanogr. 40 (8), 1802–1818. http://dx.doi.org/10.1175/2010JPO4055.1.

Chavanne, C.P., Klein, P., 2010. Can oceanic submesoscale processes be observed with satellite altimetry? Geophys. Res. Lett. L22602. http://dx.doi.org/10.1029/2010GL045057.

Chelton, D.B., DeSzoeke, R.A., Schlax, M.G., Naggar, K.E., Siwertz, N., 1998. Geophysical variability of the first baroclinic Rossby radius of deformation. J. Phys. Oceanogr. 28, 433–460. http://dx.doi.org/10.1175/1520-0485(1998)028<0433:GVOTFB>2.0.CO;2.

Chelton, D., Schlax, M., 2003. The accuracies of smoothed sea surface height fields constructed from tandem satellite altimeter datasets. J. Atmos. Ocean. Technol. 20 (9), 1276–1302. http://dx.doi.org/10.1175/1520-0426(2003)020<1276:TAOSSS>2.0.CO;2.

Chelton, D.B., Schlax, M.G., Samelson, R.M., Farrar, J.T., Molemaker, M.J., McWilliams, J.C., Gula, J., 2019. Prospects for future satellite estimation of small-scale variability of ocean surface velocity and vorticity. 173, 256–350. http://dx.doi.org/10.1016/j.pocean.2018.10.012.

Chereskin, T.K., Rocha, C.B., Gille, S.T., Menemenlis, D., Passaro, M., 2019. Characterizing the transition from balanced to unbalanced motions in the southern California Current. J. Geophys. Res. 124 (3), 2088–2109. http://dx.doi.org/10.1029/2018JC014583.

Csanady, G.T., 1982. Circulation in the Coastal Ocean. D. Reidel Publishing Company, Boston, USA.

D'Asaro, E., Lee, C., Rainville, L., Harcourt, R., Thomas, L., 2011. Enhanced turbulence and energy dissipation at ocean fronts. Science 332 (6027), 318–322. http://dx.doi.org/10.1126/science.1201515.

Dong, J., Fox-Kemper, B., Zhang, H., Dong, C., 2020. The seasonality of submesoscale energy production, content, and cascade. Geophys. Res. Lett. 47 (6), http://dx.doi.org/10.1029/2020GL087388.

Durand, M., Fu, L.-L., Lettenmaier, D.P., Alsdorf, D.E., Rodriguez, E., Esteban-Fernandez, D., 2010. The surface water and ocean topography mission: Observing terrestrial surface water and oceanic submesoscale eddies. Proc. IEEE 98 (5), 766–779. http://dx.doi.org/10.1109/JPROC.2010.2043031.

Elipot, S., Lumpkin, R., 2008. Spectral description of oceanic near-surface variability. Geophys. Res. Lett. 35 (5), L05606. http://dx.doi.org/10.1029/2007GL032874.

Emery, W.J., Thomson, R.E., 1997. Data Analysis Methods in Physical Oceanography. Elsevier, Boston, USA.

Errico, R.M., 1980. The Partitioning of Energy Between Geostrophic and Ageostrophic Modes in a Simple Model (Ph.D. thesis). Massachusetts Institute of Technology, URL http://hdl.handle.net/1721.1/53528.

Firing, Y., Chereskin, T., Watts, D., Tracey, K., Provost, C., 2014. Computation of geostrophic streamfunction, its derivatives, and error estimates from an array of CPIES in Drake Passage. J. Atmos. Ocean. Technol. 31 (3), 656–680. http://dx.doi.org/10.1175/JTECH-D-13-00142.1.

Forget, G., Campin, J., Heimbach, P., Hill, C., Ponte, R., Wunsch, C., 2015. ECCO version 4: An integrated framework for non-linear inverse modeling and global ocean state estimation. Geosci. Model Dev. 8 (10), 3071–3104. http://dx.doi.org/10.5194/gmd-8-3071-2015.

Forget, G., Ponte, R.M., 2015. The partition of regional sea level variability. Prog. Oceanogr. 137, 173–195. http://dx.doi.org/10.1016/j.pocean.2015.06.002.

Fu, L.-L., 1983. On the wave number spectrum of oceanic mesoscale variability observed by the SEASAT altimeter. J. Geophys. Res. 88 (C7), 4331–4341. http://dx.doi.org/10.1029/JC088iC07p04331.

Fu, L.-L., 2010. Oceanography from Space. Springer, pp. 147–163, Ch. Determining ocean circulation and sea level from satellite altimetry: Progress and challenges.

Fu, L.-L., Ferrari, R., 2008. Observing oceanic submesoscale processes from space. EOS Trans. Amer. Geophys. Union 89 (48), 488. http://dx.doi.org/10.1029/2008EO480003.

Gaultier, L., Ubelmann, C., Fu, L.-L., 2016. The challenge of using future SWOT data for oceanic field reconstruction. J. Atmos. Ocean. Technol. 33 (1), 119–126. http://dx.doi.org/10.1175/JTECH-D-15-0160.1.

Gildor, H., Fredj, E., Steinbuck, J., Monismith, S., 2009. Evidence for submesoscale barriers to horizontal mixing in the ocean from current measurements and aerial photographs. J. Phys. Oceanogr. 39 (8), 1975–1983. http://dx.doi.org/10.1175/2009JPO4116.1.

Gill, A.E., 1982. Atmosphere-Ocean Dynamics. In: International Geophysics Series, vol. 30, Academic Press.

Gommenginger, C., Chapron, B., 2018. SEASTAR: A Mission to Study Ocean Submesoscale Dynamics and Small-Scale Atmosphere-Ocean Processes in Coastal, Shelf and Polar Seas. Tech. rep., National Oceanography Centre (NOC), UK.

Gommenginger, C., Chapron, B., Hogg, A., Buckingham, C., Fox-Kemper, B., Eriksson, L., Soulat, F., Ubelmann, C., Ocampo-Torres, F., Buongiorno Nardelli, B., et al., 2019. Seastar: a mission to study ocean submesoscale dynamics and small-scale atmosphere-ocean processes in coastal, shelf and polar seas. Front. Mar. Sci. 6, http://dx.doi.org/10.3389/fmars.2019.00457.

Harris, F.J., 1978. On the use of windows for harmonic analysis with the discrete Fourier transform. Proc. IEEE 66 (1), 51–83. http://dx.doi.org/10.1109/PROC.1978.10837.

Kim, S.Y., 2010. Observations of submesoscale eddies using high-frequency radar-derived kinematic and dynamic quantities. Cont. Shelf Res. 30 (15), 1639–1655. http://dx.doi.org/10.1016/j.csr.2010.06.011.

Kim, S.Y., Cornuelle, B.D., Terrill, E.J., 2009. Anisotropic response of surface currents to the wind in a coastal region. J. Phys. Oceanogr. 39 (6), 1512–1533. http://dx.doi.org/10.1175/2009JPO4013.1.

Kim, S.Y., Cornuelle, B.D., Terrill, E.J., Jones, B., Washburn, L., Moline, M.A., Paduan, J.D., Garfield, N., Largier, J.L., Crawford, G., Kosro, P.M., 2013. Poleward propagating subinertial alongshore surface currents off the U.S. West Coast. J. Geophys. Res. 118 (12), 6791–6806. http://dx.doi.org/10.1002/jgrc.20400.

Kim, S.Y., Gopalakrishnan, G., Ponte, A., 2015a. Interpretation of coastal wind transfer functions with momentum balances derived from idealized numerical model simulations. Ocean Dyn. 65 (1), 115–141. http://dx.doi.org/10.1007/s10236-014-0766-x.

Kim, S.Y., Kosro, P.M., 2013. Observations of near-inertial surface currents off Oregon: Decorrelation time and length scales. J. Geophys. Res. 118 (7), 3723–3736. http://dx.doi.org/10.1002/jgrc.20235.

Kim, S.Y., Kosro, P.M., Kurapov, A.L., 2014. Evaluation of directly wind-coherent near-inertial surface currents off oregon using a statistical parameterization and analytical and numerical models. J. Geophys. Res. 119 (10), 6631–6654. http://dx.doi.org/10.1002/2014JC010115.

Kim, S.Y., Kurapov, A.L., Kosro, P.M., 2015b. Influence of modified upper ocean stratification on coastal near-inertial currents. J. Geophys. Res. 120 (12), 8504–8527. http://dx.doi.org/10.1002/2015JC011153.

Kim, S.Y., Terrill, E.J., Cornuelle, B.D., 2008. Mapping surface currents from HF radar radial velocity measurements using optimal interpolation. J. Geophys. Res. 113, C10023. http://dx.doi.org/10.1029/2007JC004244.

Kim, S.Y., Terrill, E.J., Cornuelle, B.D., Jones, B., Washburn, L., Moline, M.A., Paduan, J.D., Garfield, N., Largier, J.L., Crawford, G., Kosro, P.M., 2011. Mapping the U.S. West Coast surface circulation: A multiyear analysis of high-frequency radar observations. J. Geophys. Res. 116, C03011. http://dx.doi.org/10.1029/2010JC006669.

Klein, P., Hua, B.L., Lapeyre, G., Capet, X., Le Gentil, S., Sasaki, H., 2008. Upper ocean turbulence from high-resolution 3D simulations. J. Phys. Oceanogr. 38 (8), 1748–1763. http://dx.doi.org/10.1175/2007JPO3773.1.

Klein, P., Isern-Fontanet, J., Lapeyre, G., Roullet, G., Danioux, E., Chapron, B., Le Gentil, S., Sasaki, H., 2009. Diagnosis of vertical velocities in the upper ocean from high resolution sea surface height. Geophys. Res. Lett. 36 (12), L12603. http://dx.doi.org/10.1029/2009GL038359.

Kosro, P.M., 2005. On the spatial structure of coastal circulation off newport, oregon, during spring and summer 2001 in a region of varying shelf width. J. Geophys. Res. 110, C10S06. http://dx.doi.org/10.1029/2004JC002769.

Kundu, P.K., Chao, S.-Y., McCreary, J.P., 1983. Transient coastal currents and inertio-gravity waves. Deep Sea Res. 30 (10), 1059–1082. http://dx.doi.org/10.1016/0198-0149(83)90061-4.

Kurapov, A.L., Erofeeva, S.Y., Myers, E., 2017. Coastal sea level variability in the US west coast ocean forecast system (WCOFS). Ocean Dyn. 67 (1), 23–36. http://dx.doi.org/10.1007/s10236-016-1013-4.

Lai, Y., Zhou, H., Yang, J., Zeng, Y., Wen, B., 2017. Submesoscale eddies in the Taiwan Strait observed by high-frequency radars: Detection algorithms and eddy properties. J. Atmos. Ocean. Technol. 34 (4), 939–953. http://dx.doi.org/10.1175/JTECH-D-16-0160.1.

Lapeyre, G., Klein, P., 2006. Dynamics of the upper oceanic layers in terms of surface quasigeostrophy theory. J. Phys. Oceanogr. 36 (2), 165–176. http://dx.doi.org/10.1175/JPO2840.1.

Largier, J.L., Magnell, B.A., Winant, C.D., 1993. Subtidal circulation over the northern California shelf. J. Geophys. Res. 98 (C10), 18147–18179. http://dx.doi.org/10.1029/93JC01074.

Lee, E.A., Kim, S.Y., 2018. Regional variability and turbulent characteristics of the satellite-sensed submesoscale surface chlorophyll concentrations. J. Geophys. Res. 123 (6), 4250–4279. http://dx.doi.org/10.1002/2017JC013732.

Lee, E.A., Kim, S.Y., 2021. An investigation of the helmholtz and wave-vortex decompositions on surface currents in a coastal region. Conf. Shelf Res. submitted for publication.

Lévy, M., Franks, P.J., Smith, K.S., 2018. The role of submesoscale currents in structuring marine ecosystems. Nat. Commun. 9 (1), 1–16. http://dx.doi.org/10.1038/s41467-018-07059-3.

Marshall, J., Adcroft, A., Hill, C., Perelman, L., Heisey, C., 1997. A finite-volume, incompressible Navier Stokes model for studies of the ocean on parallel computers. J. Geophys. Res. 102 (C3), 5753–5766. http://dx.doi.org/10.1029/96JC02775.

Mazloff, M.R., Cornuelle, B., Gille, S.T., Wang, J., 2020. The importance of remote forcing for regional modeling of internal waves. J. Geophys. Res. 125 (2), e2019JC015623. http://dx.doi.org/10.1029/2019JC015623.

McWilliams, J.C., 2016. Submesoscale currents in the ocean. Proc. R. Soc. A 472 (2189), http://dx.doi.org/10.1098/rspa.2016.0117.

Minato, S., 1983. Geostrophic response near the coast. J. Oceanogr. 39 (3), 141–149. http://dx.doi.org/10.1007/BF02070801.

Molemaker, M.J., McWilliams, J.C., Capet, X., 2010. Balanced and unbalanced routes to dissipation in an equilibrated Eady flow. J. Fluid Mech. 654, 35–63. http://dx.doi.org/10.1017/S0022112009993272.

Munk, W., 1981. Evolution of Physical Oceanography. The MIT Press, pp. 264–291, Ch. 9. Internal waves and small scale processes.

Omand, M.M., D'Asaro, E.A., Lee, C.M., Perry, M.J., Briggs, N., Cetinic, I., Mahadevan, A., 2015. Eddy-driven subduction exports particulate organic carbon from the spring bloom. Science 348 (6231), 222–225. http://dx.doi.org/10.1126/science.1260062.

Osborne, J., Kurapov, A., Egbert, G., Kosro, P., 2011. Spatial and temporal variability of the M_2 internal tide generation and propagation on the Oregon shelf. J. Phys. Oceanogr. 41 (11), 2037–2062. http://dx.doi.org/10.1175/JPO-D-11-02.1.

Osborne, J.J., Kurapov, A.L., Egbert, G.D., Kosro, P.M., 2014. Intensified diurnal tides along the Oregon Coast. J. Phys. Oceanogr. 7 (44), 1689–1703. http://dx.doi.org/10.1175/JPO-D-13-0247.1.

Pettigrew, N.R., 1981. The Dynamics and Kinematics of the Coastal Boundary Layer Off Long Island (Ph.D. thesis). Massachusetts Institute of Technology. Dept. of Meteorology and Physical Oceanography, http://hdl.handle.net/1721.1/27913.

Ponte, A.L., Cornuelle, B.D., 2013. Coastal numerical modelling of tides: Sensitivity to domain size and remotely generated internal tide. Ocean Model. 62, 17–26. http://dx.doi.org/10.1016/j.ocemod.2012.11.007.

Ponte, A.L., Klein, P., 2013. Reconstruction of the upper ocean 3D dynamics from high-resolution sea surface height. Ocean Dyn. 63 (7), 777–791. http://dx.doi.org/10.1007/s10236-013-0611-7.

Ponte, A., Klein, P., 2015. Incoherent signature of internal tides on sea level in idealized numerical simulations. Geophys. Res. Lett. 52, http://dx.doi.org/10.1002/2014GL062583.

Priestley, M.B., 1981. Spectral Analysis and Time Series. Academic Press, London.

Qiu, B., Chen, S., Klein, P., Ubelmann, C., Fu, L.-L., Sasaki, H., 2016. Reconstructability of three-dimensional upper-ocean circulation from SWOT sea surface height measurements. J. Phys. Oceanogr. 46 (3), 947–963. http://dx.doi.org/10.1175/JPO-D-15-0188.1.

Qiu, B., Chen, S., Klein, P., Wang, J., Torres, H., Fu, L.-L., Menemenlis, D., 2018. Seasonality in transition scale from balanced to unbalanced motions in the world ocean. J. Phys. Oceanogr. (2018), 591–605. http://dx.doi.org/10.1175/JPO-D-17-0169.1.

Ray, R., Cartwright, D., 2001. Estimates of internal tide energy fluxes from TOPEX/Poseidon altimetry: Central North Pacific. Geophys. Res. Lett. 28 (7), 1259–1262. http://dx.doi.org/10.1029/2000GL012447.

Richman, J.G., Arbic, B.K., Shriver, J.F., Metzger, E.J., Wallcraft, A.J., 2012. Inferring dynamics from the wavenumber spectra of an eddying global ocean model with embedded tides. J. Geophys. Res. 117 (C12), http://dx.doi.org/10.1029/2012JC008364.

Rocha, C.B., Chereskin, T.K., Gille, S.T., Menemenlis, D., 2016a. Mesoscale to submesoscale wavenumber spectra in Drake Passage. J. Phys. Oceanogr. 46 (2), 601–620. http://dx.doi.org/10.1175/JPO-D-15-0087.1.

Rocha, C.B., Gille, S.T., Chereskin, T.K., Menemenlis, D., 2016b. Seasonality of submesoscale dynamics in the Kuroshio Extension. Geophys. Res. Lett. 43 (21), 11–304. http://dx.doi.org/10.1002/2016GL071348.

Rodriguez, E., Wineteer, A., Perkovic-Martin, D., Gal, T., Stiles, B.W., Niamsuwan, N., Monje, R.R., 2018. Estimating ocean vector winds and currents using a Ka-band pencil-beam Doppler scatterometer. Remote Sens. 10 (4), 576. http://dx.doi.org/10.3390/rs10040576.

Rossby, C.-G., 1938. On the mutual adjustment of pressure and velocity distributions in certain simple current systems, II. J. Mar. Res. 1 (3), 239–263. http://dx.doi.org/10.1357/002224038806440520.

Sasaki, H., Klein, P., Qiu, B., Sasai, Y., 2014. Impact of oceanic-scale interactions on the seasonal modulation of ocean dynamics by the atmosphere. Nat. Commun. 5 (5636), 1–8. http://dx.doi.org/10.1038/ncomms6636.

Savage, A.C., Arbic, B.K., Alford, M.H., Ansong, J.K., Farrar, J.T., Menemenlis, D., O'Rourke, A.K., Richman, J.G., Shriver, J.F., Voet, G., Wallcraft, A.J., Zamudio, L., 2017a. Spectral decomposition of internal gravity wave sea surface height in global models. J. Geophys. Res. 122 (10), 7803–7821. http://dx.doi.org/10.1002/2017JC013009.

Savage, A.C., Arbic, B.K., Richman, J.G., Shriver, J.F., Alford, M.H., Buijsman, M.C., Thomas Farrar, J., Sharma, H., Voet, G., Wallcraft, A.J., et al., 2017b. Frequency content of sea surface height variability from internal gravity waves to mesoscale eddies. J. Geophys. Res. 122 (3), 2519–2538. http://dx.doi.org/10.1002/2016JC012331.

Shcherbina, A.Y., D'Asaro, E.A., Lee, C.M., Klymak, J.M., Molemaker, M.J., McWilliams, J.C., 2013. Statistics of vertical vorticity, divergence, and strain in a developed submesoscale turbulence field. Geophys. Res. Lett. 40 (17), 4706–4711. http://dx.doi.org/10.1002/grl.50919.

Shearman, R.K., 2005. Observations of near-inertial current variability on the New England shelf. J. Geophys. Res. 110, C02012. http://dx.doi.org/10.1029/2004JC002341.

Soh, H.S., Kim, S.Y., 2018. Diagnostic characteristics of submesoscale coastal surface currents. J. Geophys. Res. 123 (3), 1838–1859. http://dx.doi.org/10.1002/2017JC013428.

Springer, S.R., Samelson, R.M., Allen, J.S., Egbert, G.D., Kurapov, A.L., Miller, R.N., Kindle, J.C., 2009. A nested grid model of the Oregon Coastal Transition Zone: Simulation and comparison with observations during the 2001 upwelling season. J. Geophys. Res. 114, http://dx.doi.org/10.1029/2008JC004863.

Stammer, D., 1997. Global characteristics of ocean variability estimated from regional TOPEX/POSEIDON altimeter measurements. J. Phys. Oceanogr. 27 (8), 1743–1769. http://dx.doi.org/10.1175/1520-0485(1997)027<1743:GCOOVE>2.0.CO;2.

Strub, P.T., Allen, J.S., Huyer, A., Smith, R.L., Beardsley, R.C., 1987. Seasonal cycles of currents, temperatures, winds, and sea level over the northeast Pacific continental shelf: 35°N to 48°N. J. Geophys. Res. 92 (C2), 1507–1526. http://dx.doi.org/10.1029/JC092iC02p01507.

Strub, P.T., James, C., 2000. Altimeter-derived variability of surface velocities in the California Current System: 2. Seasonal circulation and eddy statistics. Deep-Sea Res. II 47, 831–870. http://dx.doi.org/10.1016/S0967-0645(99)00129-0.

Thomas, L.N., Tandon, A., Mahadevan, A., 2008. Ocean Modeling in an Eddying Regime. In: Geophysical Monograph Series, vol. 177, American Geophysical Union, Washington, D.C., pp. 17–38, Ch. Submesoscale processes and dynamics.

Torres, H.S., Klein, P., Menemenlis, D., Qiu, B., Su, Z., Wang, J., Chen, S., Fu, L.-L., 2018. Partitioning ocean motions into balanced motions and internal gravity waves: A modeling study in anticipation of future space missions. J. Geophys. Res. 123 (11), 8084–8105. http://dx.doi.org/10.1029/2018JC014438.

Ubelmann, C., Fu, L.-L., Brown, S., Peral, E., Esteban-Fernandez, D., 2014. The effect of atmospheric water vapor content on the performance of future wide-swath ocean altimetry measurement. J. Atmos. Ocean. Technol. 31 (6), 1446–1454. http://dx.doi.org/10.1175/JTECH-D-13-00179.1.

Ubelmann, C., Klein, P., Fu, L.-L., 2015. Dynamic interpolation of sea surface height and potential applications for future high-resolution altimetry mapping. J. Atmos. Ocean. Technol. 32 (1), 177–184. http://dx.doi.org/10.1175/JTECH-D-14-00152.1.

Uchida, T., Abernathey, R., Smith, S., 2017. Seasonality of eddy kinetic energy in an eddy permitting global climate model. Ocean Model. 118, 41–58. http://dx.doi.org/10.1016/j.ocemod.2017.08.006.

Uematsu, A., Nakamura, R., Nakajima, Y., Yajima, Y., 2013. X-band interferometric SAR sensor for the Japanese altimetry mission, COMPIRA. In: Geoscience and Remote Sensing Symposium (IGARSS), 2013 IEEE International. pp. 2943–2946.

Verdy, A., Mazloff, M., Cornuelle, B.D., Kim, S.Y., 2013. Wind-driven sea level variability on the California coast: An adjoint sensitivity analysis. J. Phys. Oceanogr. 44 (1), 297–318. http://dx.doi.org/10.1175/JPO-D-13-018.1.

Veronis, G., 1956. Partition of energy between geostrophic and non-geostrophic oceanic motions. Deep Sea Res. 3 (3), 157–177. http://dx.doi.org/10.1016/0146-6313(56)90001-6.

Walden, A., 2013. Rotary components, random ellipses and polarization: a statistical perspective. Phil. Trans. R. Soc. A 371 (1984), http://dx.doi.org/10.1098/rsta.2011.0554.

Wang, J., Fu, L.-L., Qiu, B., Menemenlis, D., Farrar, T., Chao, Y., Thompson, A.F., Flexas, M.M., 2018. An observing system simulation experiment for the calibration and validation of the surface water and ocean topography sea surface height measurement using in-situ platforms. J. Atmos. Ocean. Technol. 35, http://dx.doi.org/10.1175/JTECH-D-17-0076.1.

Williams, P.D., Haine, T.W., Read, P.L., 2008. Inertia–gravity waves emitted from balanced flow: Observations, properties, and consequences. J. Atmos. Sci. 65 (11), 3543–3556. http://dx.doi.org/10.1175/2008JAS2480.1.

Yoo, J.G., Kim, S.Y., Cornuelle, B.D., Kurapov, A.L., Kosro, P.M., 2017. A non-interpolated estimate of horizontal spatial covariance from non-orthogonally and irregularly sampled scalar velocities. J. Atmos. Ocean. Technol. 34 (11), 2407–2430. http://dx.doi.org/10.1175/JTECH-D-17-0100.1.

Yoo, J.G., Kim, S.Y., Kim, H.S., 2018. Spectral descriptions of submesoscale surface circulation in a coastal region. J. Geophys. Res. 123 (6), 4224–4249. http://dx.doi.org/10.1002/2017JC013428.